BSGF - Earth Sciences Bulletin 2023, 194, 15
© J.-P. Suc *et al.*, Published by EDP Sciences 2023
https://doi.org/10.1051/bsgf/2023013

BSGF Earth Sciences Bulletin

Available online at:
www.bsgf.fr

Special Issue Messinian Crisis, ed. Jean-Pierre Suc and Jean-Loup Rubino (Guest Editors)

Open Access

Climate and Atlantic sea-level recorded in Southwestern Spain from 6.3 to 5.2 Ma. Inferences on the Messinian Crisis in the Mediterranean.

Jean-Pierre Suc[1,*], Séverine Fauquette[2], Sophie Warny[3], Gonzalo Jiménez-Moreno[4] and Damien Do Couto[1]

[1] Sorbonne Université, CNRS-INSU, Institut des Sciences de la Terre, ISTeP UMR 7193, 75005 Paris, France
[2] ISEM, Univ. Montpellier, CNRS, IRD, EPHE, Montpellier, France
[3] Department of Geology and Geophysics and Museum of Natural Science, Louisiana State University, Baton Rouge, LA, USA
[4] Departamento de Estratigrafía y Paleontología, Universidad de Granada, Avenida Fuentenueva s/n, 18002 Granada, Spain

Received: 5 December 2022 / Accepted: 25 September 2023 / Publishing online: 6 December 2023

Abstract – The Mio-Pliocene succession of Andalusia on the Atlantic coast (Guadalquivir Basin) is known as one of the former stratotype candidate for the Andalusian Stage, proposed during the seventies as the last stage of the Miocene. Its type section is located in Carmona, east of Seville. Our investigation includes the drilling of three cored boreholes, which provide bio- and magnetic-stratigraphic data in complement to pre-existing industrial information, and a high-resolution palynological analysis (pollen grains, spores and dinoflagellate cysts). The pollen flora and its climatic quantification provide the mean to correlate the section to the oxygen isotope curve from the Montemayor-1 borehole, located about 80 km to the West of Carmona. The variations in the ratio between dinoflagellate cysts and pollen grains are used to identify high and low oceanic levels, consistently with a recent paleobathymetric reconstruction based on foraminifera: the two lowest levels being successively marked by the deposit of a littoral calcarenite (the Calizza Tosca Formation) then by a subaerial erosive episode. Based on the correlation with the Montemayor-1 regional drilling, the two major lowerings in oceanic level observed at Carmona are linked with the two episodes of the Messinian Crisis. The interlocking position of the high-energy sandstone deposits inscribed in the Messinian valley leads to an assessment of a drop in the global oceanic level of about 114 m at the beginning of the paroxysm of the Messinian Crisis, amplitude to be moderated with respect to the potential effect of isostatic readjustements due to the Messinian Crisis. Comparisons are discussed with the amplitude of the Messinian Erosional Surface in the West-Alboran Basin which potentially remained suspended and fed with Atlantic waters during the height of the crisis and isolated from the rest of the almost totally dried Mediterranean Basin. The quantified climate constructed from the pollen records confirms that dry conditions existed before the Messinian Crisis in Southern Mediterranean latitudes including the Atlantic side, making the Mediterranean Sea climatically predisposed to desiccation. Atlantic sea-level variations observed in the Guadalquivir region and measured at Carmona suggest that global glacio-eustatism somewhat facilitated the onset and completion of the Messinian Crisis in the Mediterranean Basin. At last, this work allows to discriminate two regional erosive events: the first one, dated at 5.60 Ma, of fluvial origin in relation with global eustasy; the second one, submarine, occurred just before 5.33 Ma, and referred to the strain exerted by the Guadalquivir olistostrome.

Keywords: Stratigraphy / palynology / climate / climatostratigraphic relationships / sea-level changes / two steps of the Messinian Crisis

Résumé – Climat et niveau de l'océan Atlantique restitués en Espagne du Sud-Ouest de 6,3 à 5,2 Ma. Implications sur la Crise messinienne en Méditerranée. La succession mio-pliocène d'Andalousie atlantique (bassin du Guadalquivir) est connue comme ancienne candidate pour le stratotype de l'Andalousien, proposé comme dernier étage du Miocène dans les années 70. Sa coupe-type est située à Carmona, à l'est de Séville. Nos travaux comprennent notamment la réalisation de trois forages carottés où

*Corresponding author: jeanpierre.suc@gmail.com

furent acquises des données bio- et magnéto-stratigraphiques complémentaires aux informations connues des recherches industrielles et, surtout, une analyse palynologique (grains de pollen et kystes de dinoflagellés) à haute résolution. La flore pollinique et la quantification climatique autorisent des corrélations climatostratigraphiques avec la courbe $\delta^{18}O$ du forage Montemayor-1 implanté près de Huelva. Les variations du rapport entre kystes de dinoflagellés et grains de pollen permettent d'identifier les hauts et bas niveaux océaniques en accord avec une récente estimation paléobathymétrique basée sur les foraminifères, les deux plus bas niveaux étant successivement marqués par le dépôt d'une calcarénite littorale (Formation de la Caliza Tosca) puis par un épisode érosif subaérien. Après corrélation avec le forage Montemayor-1, ces deux baisses du niveau océanique sont respectivement mises en correspondance avec les deux temps de la Crise messinienne. L'emboîtement des dépôts gréseux à haute énergie inscrits dans la vallée messinienne conduit à évaluer une chute du niveau atlantique d'environ 114 m lors du paroxysme de la Crise messinienne, amplitude à modérer toutefois compte tenu du possible effet des rebonds isostatiques liés à la Crise messinienne. Des comparaisons sont discutées avec l'ampleur de l'érosion messinienne dans le bassin ouest-Alboran potentiellement resté suspendu et alimenté en eaux atlantiques pendant le paroxysme de la crise et isolé du reste du bassin méditerranéen quasi-totalement asséché. Les restitutions quantifiées du climat comparées entre la province atlantique et le domaine méditerranéen confirment les conditions xériques des latitudes sud-méditerranéennes *s.l.* et ainsi la prédisposition climatique de la Méditerranée à la dessiccation. Les variations du niveau atlantique observées dans la région du Guadalquivir et mesurées à Carmona suggèrent que le glacio-eustatisme global a quelque peu contribué au déclenchement et à l'achèvement de la Crise messinienne en Méditerranée. Ce travail permet enfin de discriminer deux événements érosifs régionaux : le premier à 5,60 Ma, d'origine fluviatile en relation avec l'eustatisme global, le second intervenu peu avant 5,33 Ma, sous-marin, lié aux contraintes exercées par l'olistostrome du Guadalquivir.

Mots-clés : Stratigraphie / palynologie / climat / correlations climatostratigraphiques / variations du niveau oceanique / deux stades de la Crise messinienne

1 Introduction

The geologic study of the Eastern Atlantic Rabat and Guadalquivir basins, located at a latitude included within the Mediterranean extent, provides a way to compare events that occurred in the Atlantic and Mediterranean domains during the time-interval encompassing the Messinian Crisis (MC) and in particular to better estimate the contribution of climate and global sea-level changes to the crisis. However, significant but somewhat controversial information on the role of climate was shown by extensive research projects on the Rabat Basin, which did not document the amplitude of sea-level changes (Hodell *et al.*, 1994; Warny and Wrenn, 1997; Warny *et al.*, 2003; van der Laan *et al.*, 2005, 2006, 2012).

The most accurate chronology of the MC has been proposed by Gautier *et al.* (1994) followed by Krijgsman *et al.* (1999), placing the crisis within the paleomagnetic Chron C3r, with its onset dated at 5.97 Ma (Manzi *et al.*, 2013), and clearly subdivided (Clauzon *et al.*, 1996) into a first (peripheral and limited) step from 5.97 to 5.60 Ma (Krijgsman *et al.*, 2001; Clauzon *et al.*, 2015a) and a second (central and paroxysmal) step from 5.60 to 5.46 Ma, ended by a sudden and dramatic reflooding by marine waters preceding the beginning of Pliocene (Bache *et al.*, 2012; Popescu *et al.*, 2021), that has finally been accepted (van Dijk *et al.*, 2023).

A crucial scientific improvement concerns the age of the closure of the Rifian Corridor now clearly dated before the onset of the MC (Achalhi *et al.*, 2016; Capella *et al.*, 2018), resulting in a corrected paleogeographic reconstruction with a Gibraltar Strait pre-existing the crisis (Krijgsman *et al.*, 2018), also completed by the proposal of a perched marine Western Alboran Basin (WAB) isolated from the almost completely desiccated Mediterranean Basin during the paroxysm of the crisis (Booth-Rea *et al.*, 2018) (Fig. 1A–B). As claimed by these authors, this paleogeographic outline is the only potential explanation to the trans-crisis survival of the Mediterranean benthic marine biota (Néraudeau *et al.*, 1999, 2001; Néraudeau, 2007), at one condition that this small basin was semi-isolated from the Atlantic Ocean by lands prefiguring the modern Gibraltar Strait as conceived in Figure 1A-B.

This novel paleogeographic context and the promising potential correlations of the Mediterranean with the high-resolution study of the boreholes Montemayor-1 and Huelva-1 cored in the Western Guadalquivir Basin (Jiménez-Moreno *et al.*, 2013; van den Berg *et al.*, 2018) led us to re-visit and re-evaluate past field work in the region of Carmona including a coring campaign (Fig. 2) done between 1987 and 1999, and the palynological results and paleoclimatic reconstructions performed on the Carmona sediments since that time. These new data are compared to those from previously published pollen records covering the same time-interval (Fig. 1C; Fauquette *et al.*, 2006; Jiménez-Moreno *et al.*, 2013).

2 Stratigraphic framework and new observations

Our research focused first on the Carmona stratigraphic succession (Fig. 3) that represents the upper part of the proposed 'Andalusian' Stage as potential equivalent to an interval running from the mid-Tortonian to the early Zanclean including the entire Messinian (Aguirre *et al.*, 1967; Perconig, 1974). This succession is made up of blue marls (thickness: ~120 m) overlain by yellow sands including thin marly beds

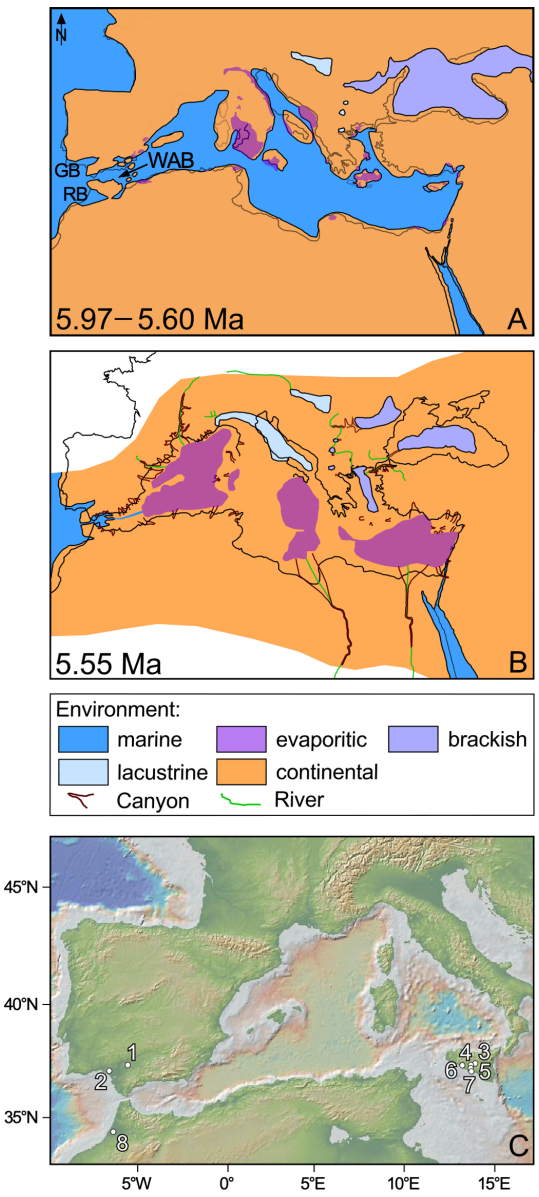

Fig. 1. The Mediterranean region. A-B: Paleogeographic reconstruction of the Northeastern Atlantic and Mediterranean regions up to the Central Paratethys during the two steps of the Messinian Crisis: A, first (peripheral and limited) step; B, second (central and paroxysmal) step (Clauzon *et al.*, 1996). These maps (modified from Suc *et al.*, 2019) consider the occurrence of the volcanic arc proposed by Booth-Rea *et al.* (2018) and the resulting perched marine isolated basin in the Western Alboran Sea connected to the Atlantic Ocean by the pre-existing Gibraltar Strait (Krijgsman *et al.*, 2018). GB, Guadalquivir Basin; RB, Rabat Basin; WAB, Western Alboran Basin.C: Location of the pollen localities considered in this paper.1, Carmona; 2, Montemayor-1; 3, Capodarso; 4, Racalmuto; 5, Realmonte; 6, Eraclea Minoa; 7, Capo Rossello; 8, Bou Regreg.The map is elaborated using GeoMapApp (Ryan *et al.*, 2009).

Fig. 1. A–B: Paléogéographie des régions nord-est atlantique et méditerranéenne pendant la Crise messinienne : A, épisode périphérique ; B, épisode paroxysmal. C, Localités polliniques.

(~20 m), followed by a beige coarse detritic aggregate called Caliza Tosca or also 'Alcor' (up to 60 m), and finally topped by greenish marls (~100 m). This succession is biostratigraphically constrained by planktonic foraminifera and calcareous nannoplankton, which evidence the foraminifer biozones N17 and N18 and the nannoplankton biozones NN11 and NN12 (Berggren and Haq, 1976), *i.e.* corresponding in terms of modern biochronology to a time interval ranging from ~8.58–8.12 to ~5.33–5.28 Ma (Anthonissen and Ogg, 2012). As major bio-events pointed out by Berggren and Haq (1976), the first occurrence of *Discoaster quinqueramus* is found in the lowermost section up to just below the base of the Caliza Tosca, and *Globorotalia margaritae* has been recorded within the greenish marls. Conversely, Sierro *et al.* (1990, 1993 1996) evidenced the first regular occurrence of *G. margaritae* ~20 m below the base of the Caliza Tosca, a bio-event now accurately dated at 6.08 Ma in the Atlantic Province (Anthonissen and Ogg, 2012). The chronologic and paleomagnetic ascriptions considered by Sierro *et al.* (1993, 1996) have been corrected by Pérez-Asensio *et al.* (2012) after considering the revised biomagneto-stratigraphy and cyclostratigraphy of the Messinian Crisis (Gautier *et al.*, 1994; Clauzon *et al.*, 1996; Krijgsman *et al.*, 1999). Considering that the first regular occurrence of *G. margaritae* in the Atlantic Province (6.08 Ma) occurred before the paleomagnetic reversal C3An.1n – C3r (6.03 Ma) and that the coiling sinistral to dextral change in *Neogloboquadrina acostaensis* (event located below the Chron C3An.1n and dated at 6.37 Ma; Anthonissen and Ogg, 2012) was not recorded within the Carmona blue marls (Sierro *et al.*, 1993, 1996), it can be concluded that the latter formation entirely belongs to Chron C3An.1n and is thus comprised between 6.25 and 6.03 Ma (Ogg, 2012). The yellowish coarse-grained Caliza Tosca is mostly made of shell fragments with abundant large *Ophiomorpha* burrows (Aguirre *et al.*, 1967; Sierro *et al.*, 1990). A rough paleobathymetric interpretation of this succession is provided by Berggren and Haq (1976) on the basis of benthic foraminifera, interpreting changing water depths of more than 150 m in the lower blue marls to about 30 m in the Caliza Tosca before increasing again around 150 m in the overlying greenish marls.

During our field trip in 1987, we observed a hard sandstone formation northeast of Carmona (Fig. 3) made up of high-energy deposits, devoid of fossil macroremains, reminiscent of an intense tide activity (Fig. 4A). This formation, which culminates at the altitude of 184 m, clearly differs from the Caliza Tosca, which culminates at the altitude of 253 m (Figs. 4B–C). We thus considered this sandstone deposit as a valley-fill within the marly succession topped by the Caliza Tosca, assumption that was fully confirmed by the coring campaign (see below). We must recall that Aguirre *et al.* (1967) reported on the basis of the Carmona geological map (Berrero Dominguez and Roldán García, 1985) that a second series made of yellow fine sands and a 'Caliza Tosca'-like formation overlays the Caliza Tosca. Such a repeated succession, which is not in chronological contradiction with our geomorphological interpretation, has been discarded because of the regional tectonic activity (Aguirre *et al.*, 1967) illustrated by the intrusive nearby Guadalquivir olitostrome (Magné and Viguier, 1974; Perconig and Martínez-Fresneda, 1977; Berrero Dominguez and Roldán García, 1985; Martínez del Olmo and

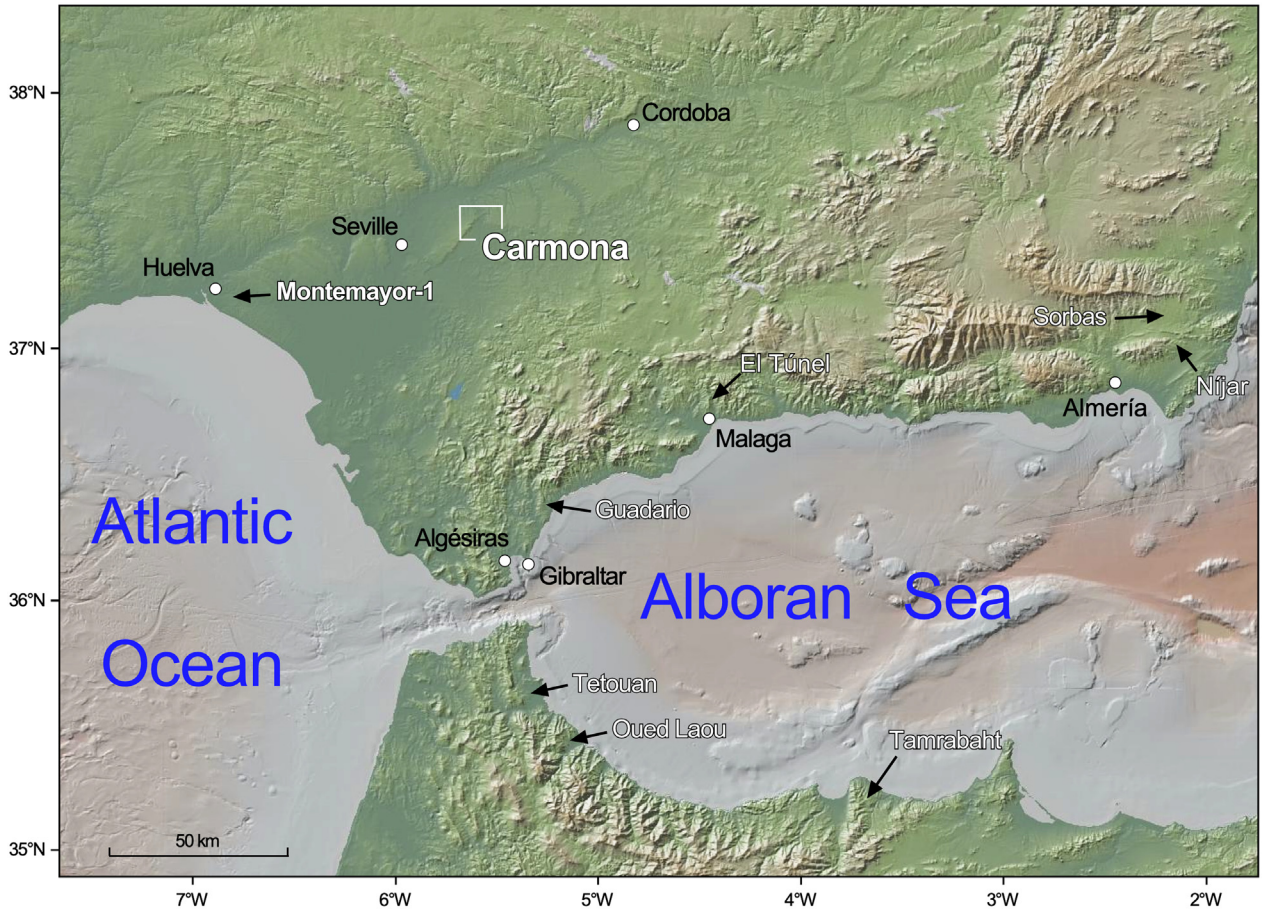

Fig. 2. Regional topographic map showing the study area (Carmona) and other locations considered for stratigraphic comparison. The map is elaborated using GeoMapApp (Ryan *et al.*, 2009).
Fig. 2. Localisation du secteur de Carmona et des autres sites régionaux considérés.

Sánchez, 2019). This interpretation led Berrero Dominguez and Roldán García (1985) to hypothesize an underground fault (Fig. 3A), without neither field nor underground evidence (Ledesma, 2000), probably to explain the difference in altitude that we refer to fluvial erosion. Aguirre *et al.* (2015) carried out a sedimentological, micropaleontological and geochemical study of the Caliza Tosca calcarenite that, following the interpretation of the Carmona geological map (Berrero Dominguez and Roldán García, 1985), they stratigraphically correlated with the sandstone formation here above described from the same location that they called the 'Carmona Quarry' section (location 1 in Fig. 3A). The lithological description and the photographs as well as the benthic foraminifer fauna composition published by Aguirre *et al.* (2015) obviously show that the 'Carmona Quarry' section significantly differs from two locations below the Carmona city (Carmona Antena and Carmona Fútbol sections, locations 2 and 3 in Fig. 3A, respectively). In addition, the high-energy setting concluded by Aguirre *et al.* (2015) for the 'Carmona Quarry' section supports the distinction of this section from those below Carmona (Carmona Antena and Carmona Fútbol).

The above-mentioned Guadalquivir olistostrome is a huge volume of resedimented chaotic material originating from the northern side of the Betic Cordillera characterized by a progressive northward penetration beneath the marine Guadalquivir Basin (Vera, 2000; Civis *et al.*, 2004). Its outline, thickness and depth within Tortonian to early Messinian sediments are known thanks to many industrial seismic profiles and boreholes (Ledesma, 2000; Martínez del Olmo and Sánchez, 2019). This unit is nowadays exposed near Carmona and its tip is located at about 6 km southward the city at ca. 400 m in depth (Ledesma, 2000). Its sliding occurred during the late Tortonian with an almost continuous thrusting for 9 Ma.

Fortunately, the interpretation of the Montemayor-1 borehole in terms of changes in sea level in correlation with the Messinian Crisis in the Mediterranean (Jiménez-Moreno *et al.*, 2013; Pérez-Asensio *et al.*, 2013; Pérez-Asensio, 2021) highlights the importance of the data acquired from the Carmona boreholes and outcrops and their revaluation.

3 Methods

One hundred fifteen samples were collected along the exposed blue marls underlying the Caliza Tosca (section A in Fig. 3B: altitude range: 125–185 m; thickness: 62 m), 66 of them yielded pollen grains and dinoflagellate cysts in enough quantity for a detailed quantitative analysis. Forty samples were collected in borehole D cored through the greenish marls

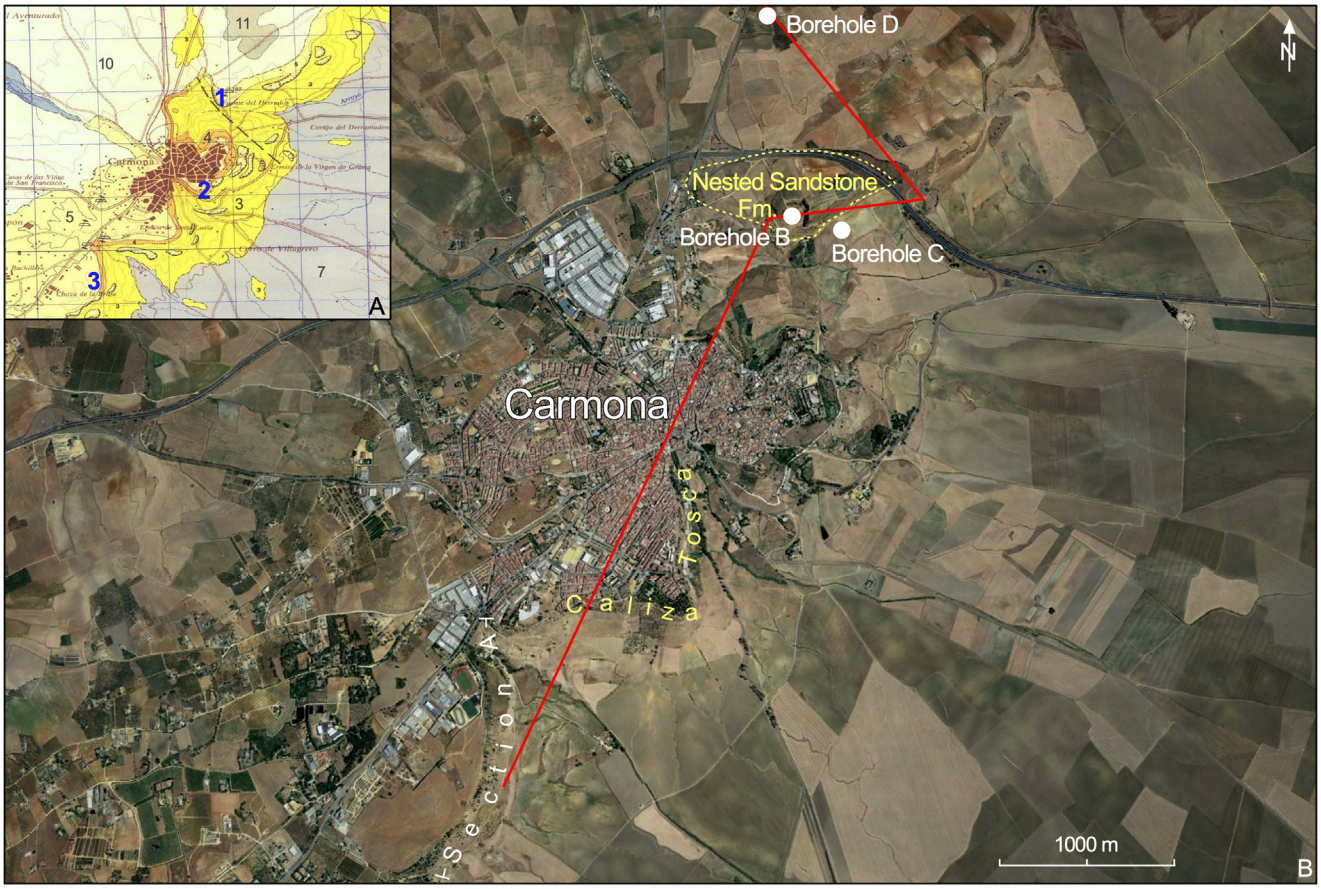

Fig. 3. The Carmona area. A, Geological map of the Carmona area at scale 1:50,000 (Borrero Dominguez and Roldán García, 1985).Localities studied by Aguirre *et al.* (2015): 1, Carmona Quarry; 2, Carmona Antena; Carmona Fútbol.Geological units: 3, Upper Tortonian marls. Messinian: 4, alternating blue marls and calcarenite; 5, sandy calcarenite. Quaternary: 7, grey clays; 10, conglomerates and sands; 11, clays and loams.B, Google Earth image of the Carmona area with the Caliza Tosca calcarenite, the Nested Sandstone Formation, and the studied exposed section (A) and boreholes (B, C, and D).Red broken line: composite cross-section shown in Figure 5.
Fig. 3. A, Carte géologique du secteur de Carmona avec les coupes décrites par Aguirre *et al.* (2015). B, Localisation des coupes de notre étude (ligne brisée rouge : coupe détaillée de la Figure 5).

(23 m in thickness) locally covered by 3 m of Quaternary loams (Fig. 3B). Sixteen of these samples provided pollen grains and dinoflagellate cysts in enough quantity. About 20-30 grams have been processed per sample in order to obtain pollen using the classical method (acid digestions with hydrochloric acid (HCl) and hydrofluoric acid (HF), concentration in $ZnCl_2$ at density 2, and sieving at 10 μm). In all the analyses (see Tab. S1 for details), a minimum of 100 pollen grains in addition to pollen grains of *Pinus* (because they are often overrepresented in marine sediments) and 300 dinoflagellate cysts were counted per sample with a few exceptions (for detailed analyses, refer to Warny 1999). The summary pollen diagrams are established on a pollen sum excluding *Pinus* and indeterminable Pinaceae. The 'dinoflagellate cysts/pollen grains' ratio (D/P) is established using the total of dinoflagellate and acritarch cysts vs. the total of pollen grains (including *Pinus* and indeterminable Pinaceae). The D/P ratio is useful for determining sea-level changes (D/P>1 for sea-level rise, D/P<1 for sea-level fall; Warny *et al.*, 2003). However, the coastal context of the two considered locations (Camona sections and Montemayor-1 hole) may somewhat lessen its significance, for example when pollen transport is intensified by river floods.

The Climatic Amplitude Method was used to reconstruct climate conditions during the deposition of the sediments. This method, after comparison with more than 6,000 present-day pollen records distributed worldwide, relies on the relationship between the relative abundance of each individual taxon and the climate because the method accounts not only for the presence/absence criterion but also percentages (Fauquette *et al.*, 1998). The estimated mean annual temperatures (MAT), mean temperatures of the coldest (MTC) and warmest (MTW) months and mean annual precipitation (MAP) (Tab. S2) focus on low-elevation vegetation because meso-microthermal and microthermal taxa (*Cedrus*, *Fagus*, *Tsuga*, *Cathaya*, *Abies* and *Picea* which live today at higher elevations in tropical-subtropical regions) are excluded from the process (but not from the percentages) to avoid a cold bias linked to transport from higher elevations. *Pinus*, which may inhabit different vegetation belts, is also excluded from the calculation. The

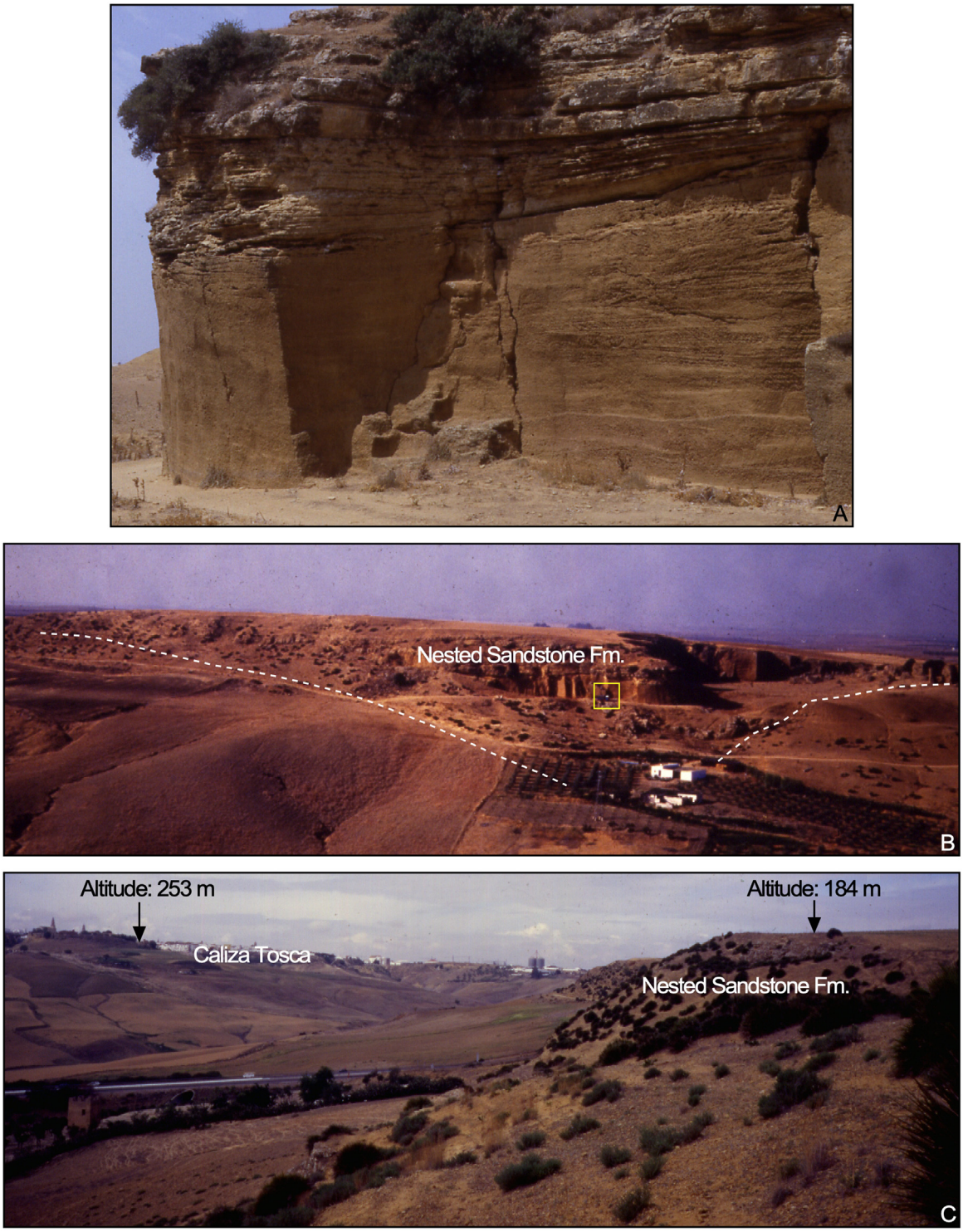

Fig. 4. Photographs of the Carmona area showing the Nested Sandstone Formation and its relationships with the Carmona classical succession. A, Facies of the Nested Sandstone Formation; B, Relationship between the Nested Sandstone Formation and the Carmona blue marls emphasized by a dotted white line. The yellow square highlights the location of the drilling rig in the quarry at the foot of the cliff – borehole B); C, Respective altitude of the top of the Caliza Tosca and the Nested Sandstone Formation. Photographs by J.-P. Suc.
Fig. 4. Emboîtement de la formation gréseuse de Carmona. A, Faciès de cette formation. B, Emplacement de notre forage B. C, Comparaison altimétrique avec la Caliza Tosca.

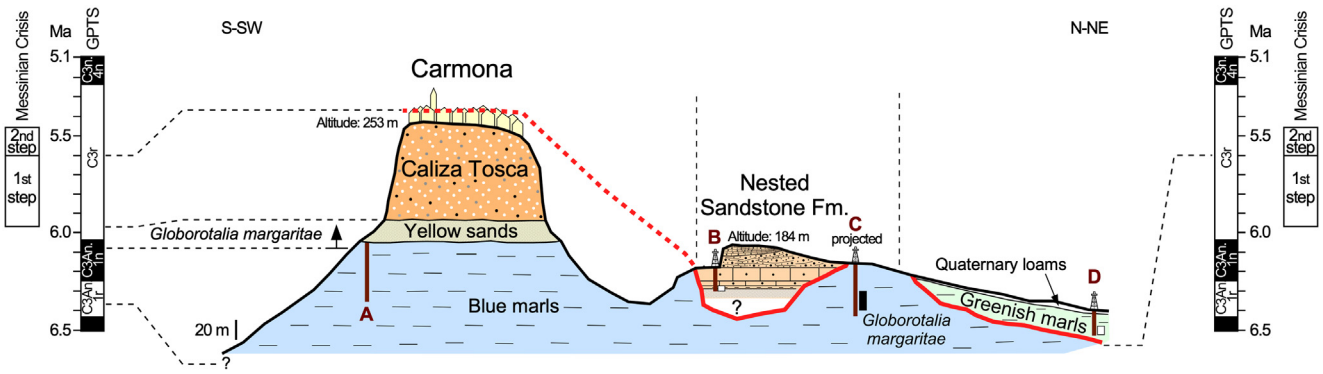

Fig. 5. Morphologically and chronologically interpreted cross-section of the Carmona area including the exposed studied section A and the three cored boreholes (B-D) with biostratigraphic and paleomagnetic information (white: reverse polarity; black: normal polarity).Red (dotted or continuous) line: inferred subaerial erosional surface Vertical dotted lines: changes of direction of the broken line shown in Figure 4B.Global polarity time scale (GPTS) from Ogg (2012).

Fig. 5. Interprétation morphographique et chronostratigraphique de la coupe de Carmona avec positionnement de nos trois forages et tracé (en rouge) de la surface d'érosion subaérienne.

estimates for each climatic parameter are given as an interval (minimum and maximum values of the parameter) and a most likely value (MLV) corresponding to a weighted mean (Tab. S2). The MLV has been statistically tested on modern pollen data and has provided reliable results (Fauquette *et al.*, 1998).

Three boreholes were cored using the Sedidrill engine equipped with a cable sampler of the *Laboratoire de Botanique Historique et Palynologie* (Aix-Marseilles University) (Fig. 3B): B (top altitude: 164 m; depth: 25 m; photographs of Fig. 4A-B show the place where this hole was cored), C (top altitude: 163 m; depth: 58 m); D (top altitude: 125 m; depth: 26 m). Paleomagnetic logging was performed within boreholes using the experimental material perfected by the *Laboratoire d'Electronique, de Technologie et d'Instrumentation* (*LETI-CEA*, Grenoble) then compared in Grenoble with measurements made on oriented cores using a test bed (Pozzi *et al.*, 1993).

As reference for the time-interval 6.40–5.20 Ma, we use the oxygen isotope curve of the Montemayor-1 hole which benefits from an accurate correlation with ATNTS2012 of Hilgen *et al.* (2012). As reference chronological points, we particularly considered base and top of Chron C3An.1n, isotope stages TG22, TG12 and TG7, and base of Chron C3n.4n, following the time-model of Pérez-Asensio *et al.* (2013) and Jiménez-Moreno *et al.* (2013)

4 Chronostratigraphic model

As noted above, the biostratigraphic data demonstrate that the exposed section A (blue marls) must be correlated with the normal Chron C3An.1n (Fig. 5). The overlying yellow sands and Caliza Tosca obviously illustrate a significant lowering of sea level. Strong differences in facies and altitudinal gap (Fig. 4C) show that the sandstone formation exposed northeast of Carmona cannot be linked to the Caliza Tosca. This sandstone deposit pinches on both sides of the quarry where borehole B was drilled suggesting the morphology of a paleovalley (Fig. 4B). This deposit is hereafter referred as the Nested Sandstone Formation. Such a morphological interpretation is supported (1) by the depth reached in borehole B through sandstones without passing to the expected underlying blue marls (the five lowermost meters being composed of clays alternating with sands) (Fig. 5), and (2) by the very close borehole C drilled within a blue marl succession along 58 m characterized by the continuous occurrence of *Globorotalia margaritae* (Sierro, *in litteris*: Oct. 10, 1997). The succession cored in borehole C is considered as lateral equivalent to the topmost section A and maybe in part to the yellow sands (Fig. 5). The promising intensity of remnant magnetization detected in some parts of the drilled sections both during logging *in situ* and through measurements on cores were validated by some paleomagnetic measurements performed on isolated samples. These additional analyses show that the base of borehole B is actually reverse, most of the borehole C is normal, and the base of borehole D is reverse (Krijgsman, *in litteris*: Apr. 30, 1998). Our interpretation of the studied sections is thus supported by paleomagnetic data (Fig. 5). A regressive environment characterized the marine blue marls up to the coastal Caliza Tosca during the early Chron C3r. The section is then characterized by a well-marked erosional surface that affected the series, followed by the deposition of the Nested Sandstone Fm., which corresponds to a positive fluctuation of the sea level marked by tidal conditions finally leading to the deposition of the greenish marls biostratigraphically ascribed to Zanclean (Fig. 5; Berggren and Haq, 1976). Taking into account the altitude of the top of the Caliza Tosca (253 m) and that of the Nested Sandstone Fm. (184 m) in addition to its exposed thickness (20 m) plus the borehole B depth (25 m), an erosion of about 114 m may be inferred. All these contrasted deposits and events occurred during Chron C3r and may be, as a first hypothesis, correlated with the Mediterranean events as follows: the Caliza Tosca would be associated with the first step of the Messinian Crisis, the erosion with the second step of the Messinian Crisis, the subsequent sea-level rise represented by the Nested Sandstone Fm. with the marine reflooding of the Mediterranean that ended the

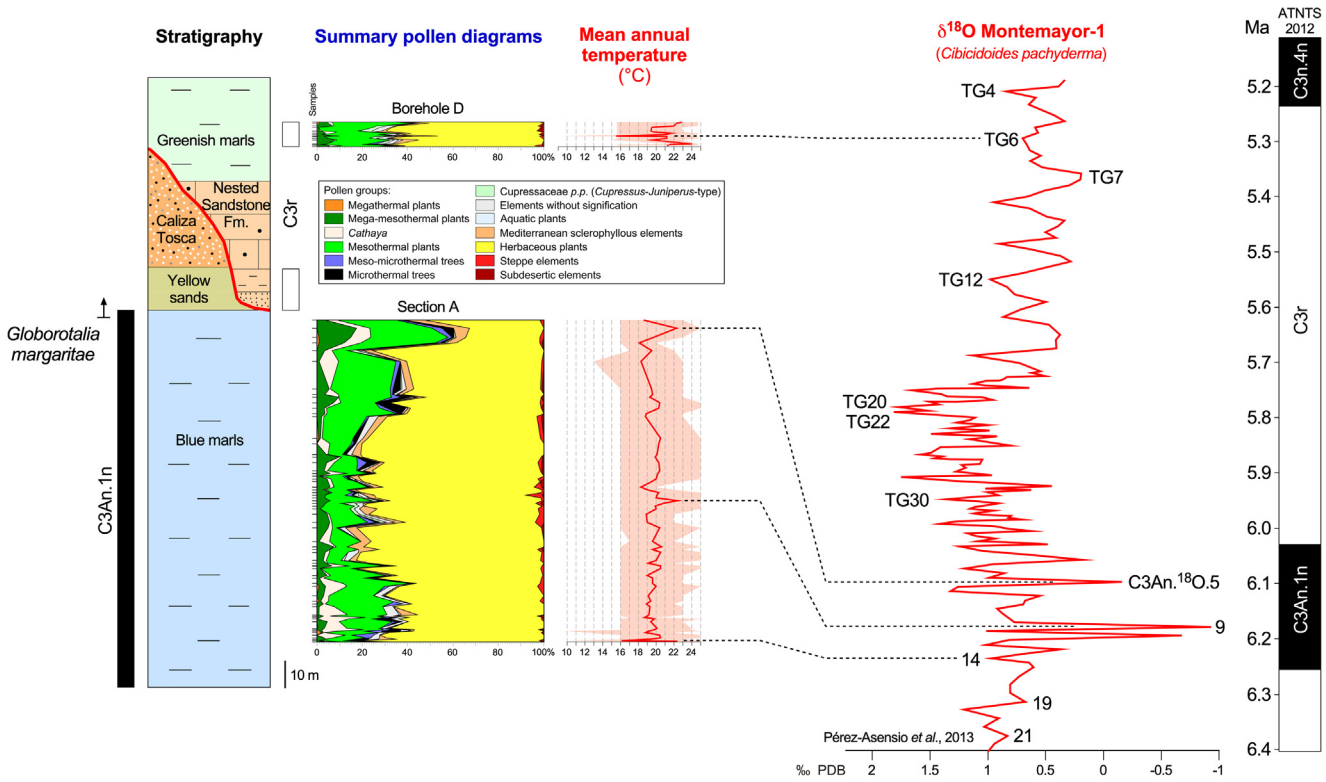

Fig. 6. Summary pollen diagrams of the Carmona series with respect to its chronostratigraphy, in parallel to the quantified mean annual paleotemperature, and proposed climatostratigraphic correlations with the oxygen isotope curve from the Montemayor-1 hole directly calibrated with ATNTS2012. Isotope stage numbering of Chron C3An refers to Hodell *et al.* (1994). ATNTS2012 refers to the Astronomically tuned Neogene time scale (Hilgen *et al.*, 2012).

Fig. 6. Diagramme pollinique synthétique de la série de Carmona avec quantification de la paléotempérature et corrélation bio-magnéto-climato-stratigraphique avec le forage Montemayor-1.

Messinian Crisis (Fig. 5). The last ascription is supported by the occurrence of some planktonic foraminifera at the base of hole B (Sierro, *in litteris*: Oct. 10, 1997).

5 Palynology, climate and climatostratigraphy

The pollen flora is constituted by 141 taxa, which have been grouped in a summary pollen diagram according to their ecological significance (Fig. 6). Pollen concentration fluctuates between 200 and 10,800 pollen grains/gram of dry sediment, and for most of the samples between 1,000 and 2,000 pollen grains/gram. Except for *Pinus*, the pollen flora is dominated by herbaceous plants (mainly Compositae and Poaceae, and in a lesser quantity Apiaceae, Brassicaceae, Amaranthaceae, Geraniaceae, *Plantago*, *Rumex*, Cyperaceae, etc.) with some steppe (*Artemisia*, *Ephedra*) and subdesertic (*Nolina*, Agavaceae, *Lygeum*, *Calligonum*, *Neurada*) elements. The Mediterranean sclerophyllous elements (*Ceratonia*, *Pistacia*, *Olea*, *Nerium*, evergreen *Quercus*, *Phillyrea*, etc.) are continuously recorded but in low percentage. Such a pollen assemblage is characteristic of the modern southern Mediterranean vegetation with open landscapes covered by prevalent herbaceous plants, the pollen grains of which are still underrepresented in pollen records (Favre *et al.*, 2008). Arboreal vegetation at low altitude is composed by a few megathermal elements (as *Canthium*-type), some mega-mesothermal elements (Arecaceae, *Engelhardia*), more frequent mesothermal elements (deciduous *Quercus*, *Acer*, *Carya*, *Juglans*, Ericaceae, etc.) including riparian trees (*Liquidambar*, *Pterocarya*, *Parrotia persica*, *Alnus*, *Fraxinus*, *Ulmus*, *Zelkova*, *Salix*, *Populus*). Some aquatic taxa are recorded in very low abundance. Forest vegetation was more developed with increasing altitude, indicated by relatively low percentages of *Cathaya* mainly, *Fagus*, *Tsuga*, *Cedrus*, and higher by *Picea* and *Abies*. The opposed variations of herbaceous plus steppic plus subdesertic plants compared to mesothermal elements suggest climate fluctuations along the Carmona succession.

Climatic parameters have been quantified using the Climatic Amplitude Method. At first sight, climate at Carmona from the latest Miocene to earliest Pliocene was on the whole warmer and almost as dry as today (present-day values: MAT: 18.6°C; MTC: 9.7°C; MTW: 28.7°C; MAP: 521 mm; source: Climate data for cities worldwide) with the MLV of MAT around 20−21°C, of MTC around 11.5°C, of MTW around 26°C, and of MAP around 550-650 mm (Tab. S2). Two minima and two maxima in MAT are remarkable and provide a potential for robust climatostratigraphic correlations with the oxygen isotope curve from the Montemayor-1 hole

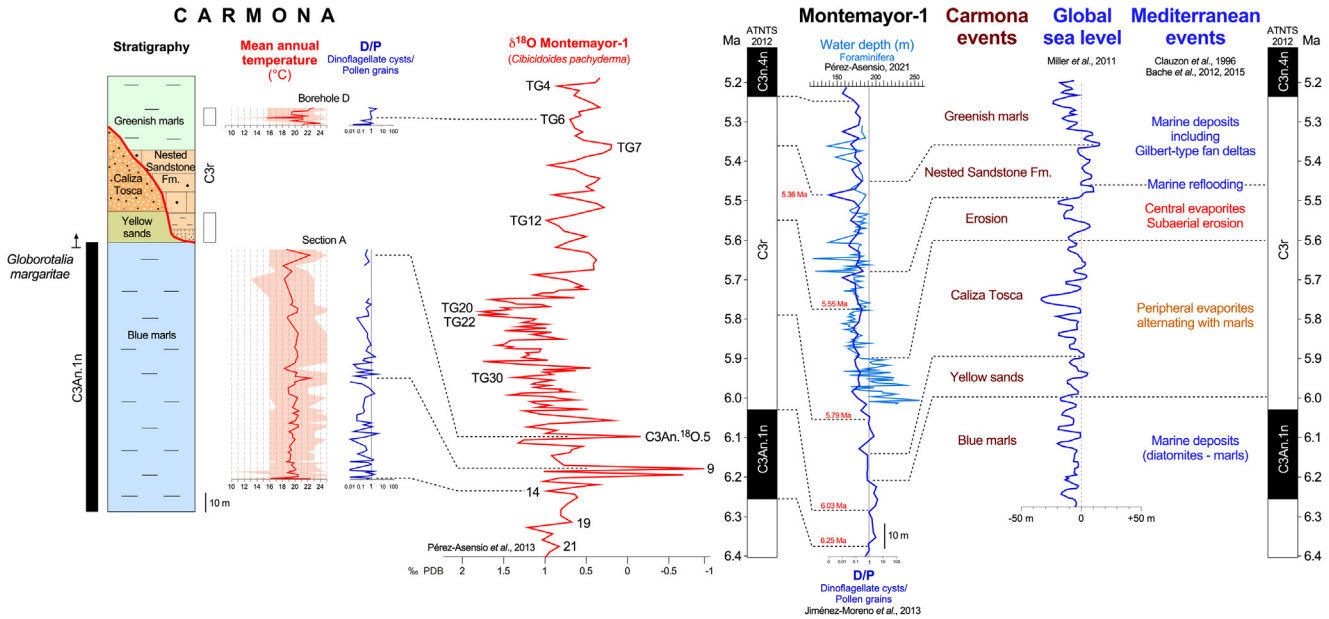

Fig. 7. Curve of the D/P ratio of the Carmona series with respect to its chronostratigraphy correlated with the Montemayor-1 oxygen isotope curve. Comparison with the D/P curve and the foraminifer-based paleobathymetric curve (Pérez-Asensio, 2021) from the Montemayor-1 hole and proposed relationships with the global sea level and Mediterranean events, all calibrated with ATNTS2012 as the oxygen isotope curve. D/P curves are drawn according to a semi-logarithmic scale.

Fig. 7. Variations du niveau marin dans le basin du Guadalquivir et correlations avec les événements méditerranéens.

(Pérez-Asensio *et al.*, 2013) with respect to chronostratigraphy of the succession (Fig. 6):

the lower cooler episode concerns the samples at the height 1.25–1.50 m in section A that we correlate with the isotope stage C3An^{18}O.14, the older oxygen maximum within the Chron C3An.1n;

– the following warmer episode is located in the middle part of section A at the thickness 27 m that we correlate with the isotope stage C3An^{18}O.9 which is the lower oxygen minimum in the mid-Chron C3An.1n;
– the next warmer episode concerns the top of section A at the thickness 58.70 m that we correlate with the isotope stage C3An^{18}O.5 which constitutes the lower oxygen minimum in the upper Chron C3An.1n;
– the upper cooler episode is located in borehole D at 21.64 m depth, correlated with isotope stage TG6, the last oxygen maximum in the Chron C3r.

Palynological records may also inform on sea-level fluctuations by using the D/P (dinoflagellate cyst total/pollen grain total) ratio, assuming that the predominance of dinoflagellate cysts over pollen corresponds to higher sea level/enhanced marine influence, while dominance of pollen grains with respect to dinoflagellate cysts may indicate low sea level in relation with increased fluvial transport from land/proximity to the coast (Warny *et al.*, 2003; Jiménez-Moreno *et al.*, 2006, 2013; Iaccarino *et al.*, 2008). Section A displays a fluctuating D/P ratio in a decreasing tendency from the base to the top (Fig. 7). Conversely, the ratio tends to increase in borehole D (Fig. 7). The D/P evolution in Carmona A and D sections is consistent with the D/P curve calculated for the Montemayor-1 hole:

– the curve is almost continuously >1 during an interval encompassing the Chron C3An.1n correlated with the blue marls of Carmona, the top of which is located at ~5.97 Ma;
– then, a stable phase (estimated from ~5.97 to ~5.89 Ma) that corresponds to the yellow sands of Carmona;
– above, D/P decreases again with minima estimated at 5.85 Ma and after 5.74 Ma; we correlate the lower part of the Caliza Tosca to this episode;
– a lowermost value of D/P is reached at ~5.50 Ma within an interval to which we refer the upper part of the erosional episode observed at Carmona;
– above this interval, we correlate the fluctuating higher sea-level to the Nested Sandstone Fm. and the greenish marls of Carmona.

6 Discussion

Here we discuss several items such as: (1) the erosional context in the area of Carmona and its relationship with tectonics and eustasy; (2) the potential correlation of the sea-level changes recorded at Carmona and at the outlet of the Guadalquivir Basin (Montemayor-1 well) with the global sea-level fluctuations (Miller *et al.*, 2011) and the events characterizing the MC in the Mediterranean Basin (Clauzon *et al.*, 1996, 2015a; Bache *et al.*, 2012) in order to elucidate which effect had the Atlantic-level fall, including a fall of at least 114 m measured at Carmona; (3) the effect of this fall in

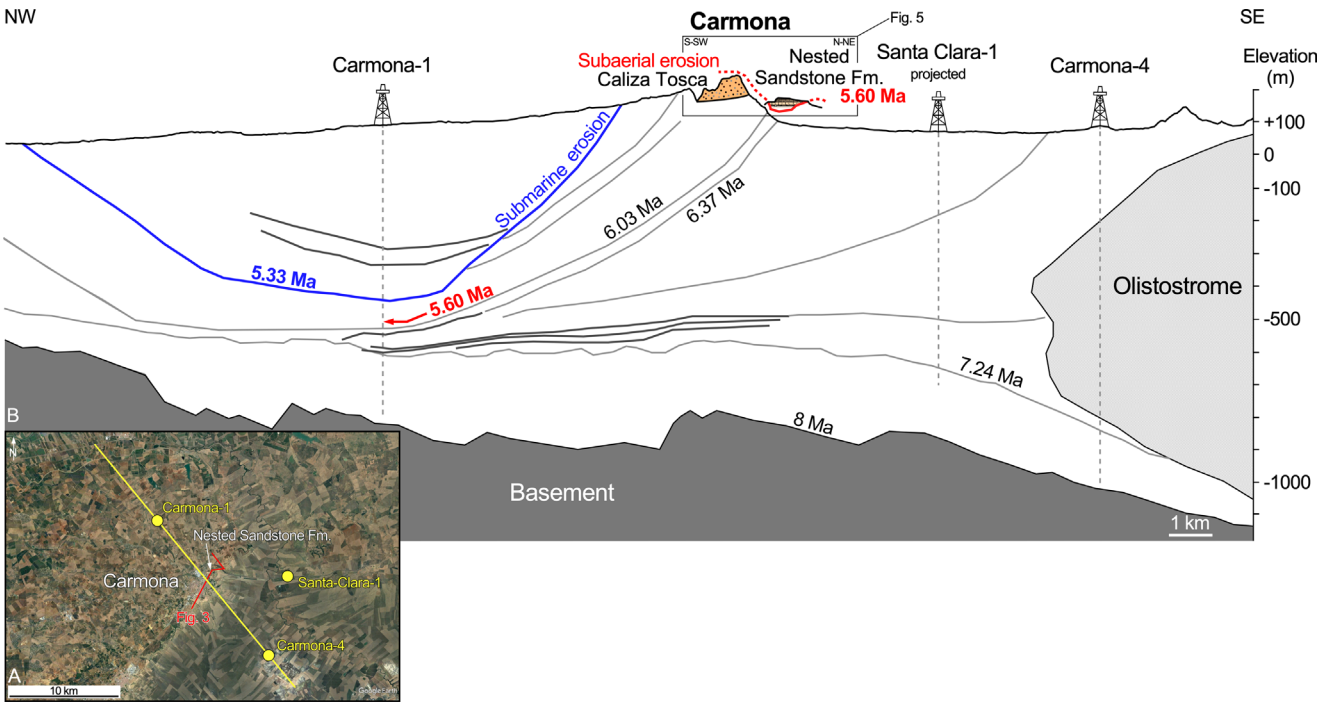

Fig. 8. Chronostratigraphy of the area of Carmona based along an industrial seismic profile including three deep industrial boreholes and this work. A, The Carmona area from Google Earth image with plotted seismic profile and industrial boreholes and location of the studied cross profile (Fig. 3).B, Interpreted seismic profile and industrial drilled sections showing the different lithostratigraphic and biostratigraphic units and their boundary age according to Ledesma (2000) - some ages are updated with respect to Hilgen *et al.* (2012) - contrasting with the studied cross profile (Fig. 5). The figure emphasizes the diverse types of erosion and their age that affected the area of Carmona in the late Messinian. The red arrow pinpoints the level of deposition in the marine basin of the eroded material from the Caliza Tosca. The light grey lines indicate sedimentary more marked reflectors. The dark grey lines indicate the thick turbiditic reflectors.
Fig. 8. Chronostratigraphie interprétée des environs de Carmona sur la base des données industrielles et de notre étude illustrant la distinction contextuelle et temporelle entre l'érosion sous-marine liée au déplacement de l'olistostrome du Guadalquivir et l'érosion subaérienne due à une baisse du niveau marin.

global sea level on the WAB which remained perched and isolated from the almost completely desiccated Mediterranean Basin during the paroxysm of the MC (Booth-Rea *et al.*, 2018); (4) the comparison of climatic conditions in regions located at similar latitude, such as the Guadalquivir area and Sicily (Fig. 1C), in order to deepen our understanding of the climate influence on the MC (Suc and Bessais, 1990; Fauquette *et al.*, 2006; Murphy *et al.,* 2009).

6.1 Erosion at Carmona: submarine vs. subaerial context? tectonic or eustatic forcing?

The intrusion of the olistostrome and its northward thrusting up to nearly Carmona at about 7–6 Ma caused the strain of the Guadalquivir Basin with a maximum compression at about 7 Ma followed by some release and subsidence at 5.33 Ma (Ledesma, 2000). The resulting strong instability of the slope led to impressive submarine erosion and well-marked turbiditic reflectors onlapping this discontinuity (Fig. 8; Ledesma, 2000; Martínez del Olmo and Sánchez, 2019). Thanks to an accurate bio-chronostratigraphic calibration of wells in the area, Ledesma (2000) established that an episode of submarine erosion occurred just before 5.33 Ma marked by a pronounced seismic reflector which truncates the older sediments, the culmination of which is estimated at an elevation −450 m in the Carmona-1 well (Fig. 8). The earliest Zanclean age ascribed to this level is supported (1) by a marked increase in planktonic foraminifers and (2) abundant glauconite (Ledesma, 2000) which is described as a widely generalized condensed bed marking the maximum marine inundation on the external shelf of the Guadalquivir Basin (Sierro *et al.*, 1996). The erosion of the Caliza Tosca (Fig. 5) is slightly older (1) because of the sideward location of the formation and (2) because the products of this erosion were recorded at elevation −506 m in the Carmona-1 well as pointed out by the red arrow in Figure 8 (Ledesma, 2000). This is consistent with the more modern age of 5.60 Ma that we propose for this erosion (Fig. 7). In addition, the erosion of the Caliza Tosca is characterized by a distinctly lesser amplitude than the submarine erosion and affected coastal shallow deposits (ca. 30 m of water depth according to Berggren and Haq, 1976), being a subaerial context thus a better setting for this erosional event. Our interpretation is supported by increased amounts of riparian trees and Pteridophyte plus fungus spores and reworked palynomorphs in the uppermost section Carmona A (*i.e.*, just below the Caliza Tosca) and in the borehole Carmona D (*i.e.*, the overlying greenish marls)

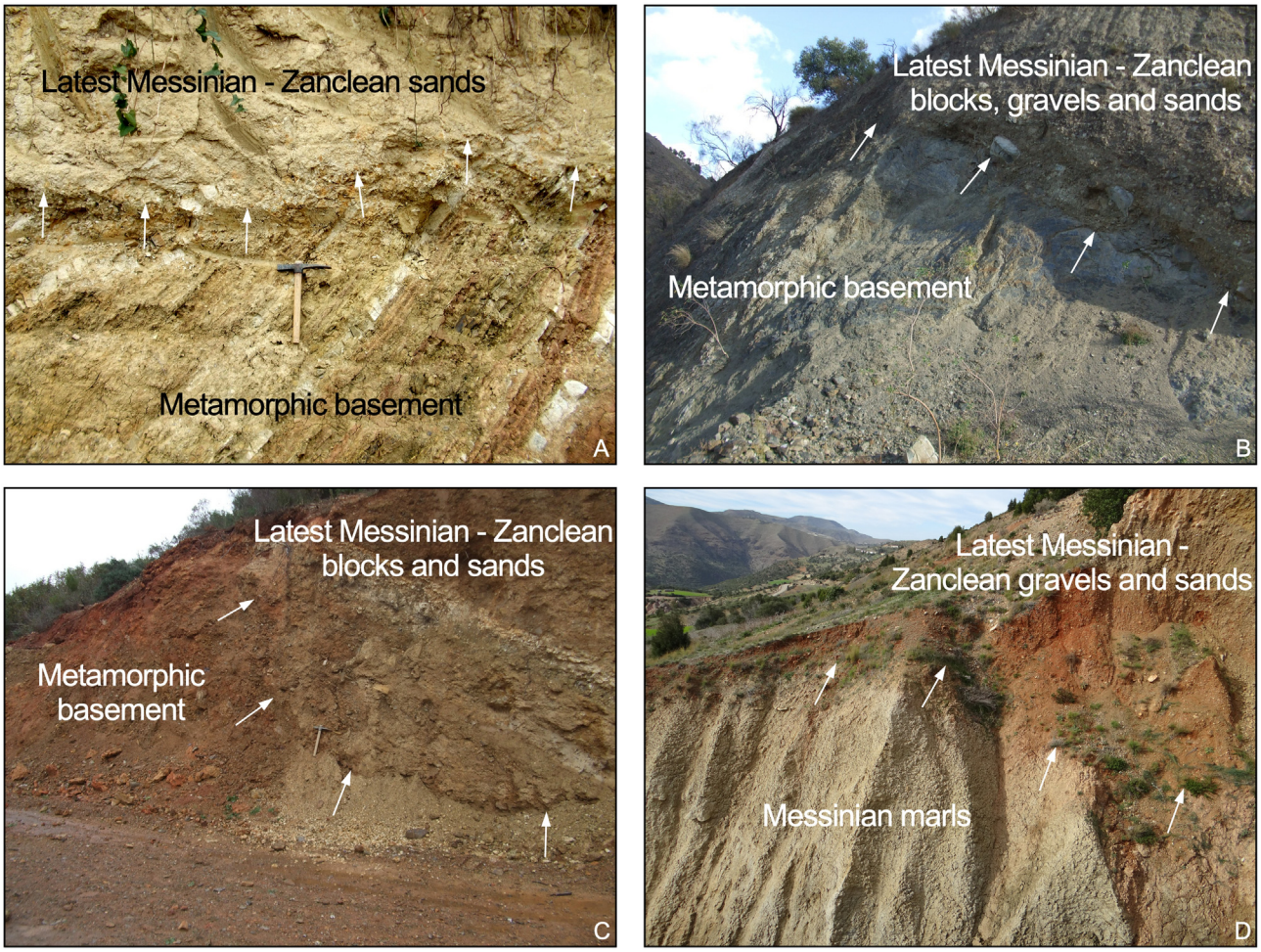

Fig. 9. Photographs of the Messinian Erosional Surface taken in four different outcrops located on both sides of the Alboran Sea.A, Guadario (Algesiras, Spain); B, El Túnel (Malaga, Spain); C, Tassafete (Oued Laou, Morocco); Tamrabaht (Boudinar, Morocco). In all outcrops, the Messinian Erosional Surface is underlined by white arrows.Photographs A-C) by J.-P. Suc, photograph D by D. Do Couto.
Fig. 9. Photographies de la Surface d'érosion messinienne sur le pourtour de la Mer d'Alboran : A, Guadario (Algesiras, Espagne); B, El Túnel (Malaga, Espagne); C, Tassafete (Oued Laou, Maroc); Tamrabaht (Boudinar, Maroc).

(Tab. S1), that attests a greater influence of river input (onset of the Guadalquivir River?) in relation with a shallower environment. A subaerial erosion is supported by the age-equivalent Vejer de la Frontera section located southeast of Cádiz, which shows an uppermost Miocene coastal marine calcarenites similar to the Caliza Tosca overlain by unconformable Zanclean sands that looks just like the Carmona surface succession (Rico-García, 2007).

We thus postulate that the two erosional events recorded at Carmona are both distinct in their nature and chronology as expressed in Figure 8. If the deep submarine erosion was controlled by the olistostrome thrusting, the surface subaerial erosion was most probably forced by a sea-level fall as also supported by the high energy of deposits filling this fluvial valley ('Carmona Quarry') marking the following rise in sea level (Fig. 4; Aguirre *et al.*, 2015). The proposed age at 5.6 Ma for this subaerial erosion (Fig. 5) suggests that the event is relevant to the MC paroxysm without discarding some effect of isostatic readjustements in the Mediterranean (Sierro *et al.*, 2008). Anyway, the influence of the olistostrome appears to be discarded for the origin of this surface erosional event. This interpretation is finally reinforced by the changes in water depth estimated by Pérez-Asensio (2021) from the foraminifer record in the Montemayor-1 well, evidencing a strong sea-level fall at 5.6 Ma followed by several successive sea-level rises from ca. 5.49 Ma (Fig. 7). We can also hypothesize that the greenish marls of Carmona, which mark the local final step of the sea-level rise, are the coastal equivalent to the turbidites overlying the submarine erosional horizon (Fig. 8).

The submarine erosion posterior to the Caliza Tosca was sometimes considered as representing the MC in the Atlantic Province (Martínez del Olmo *et al.*, 1996; Martínez del Olmo and Martín, 2016a, b). Our work here contributes to separate the erosional episode mainly linked to eustatic lowering from that exclusively due to tectonic activity.

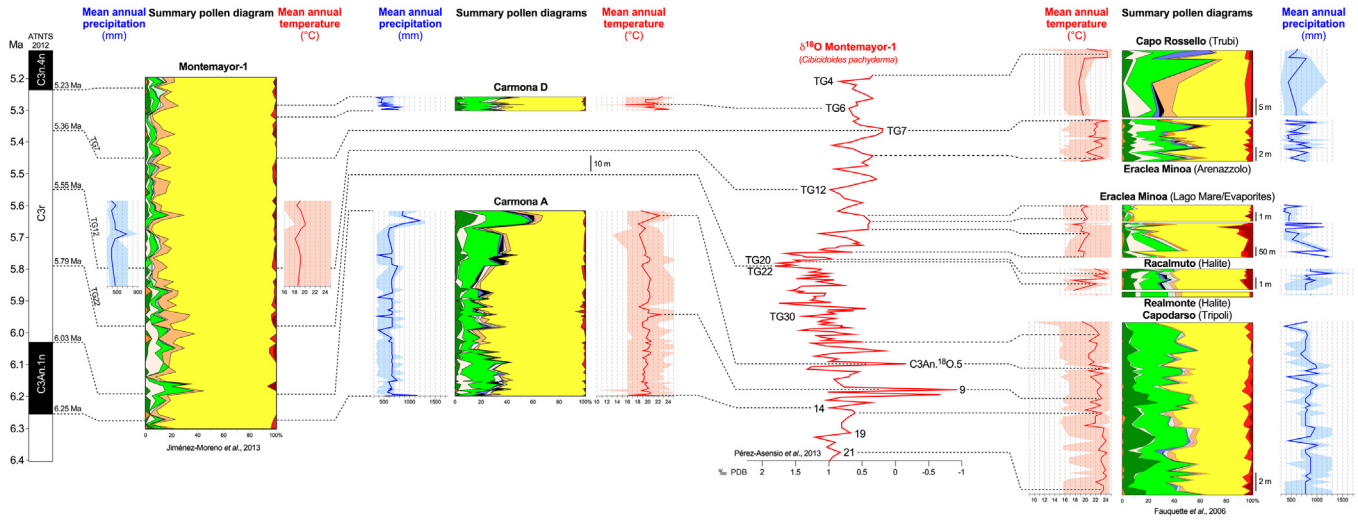

Fig. 10. Compared summary pollen diagrams from Montemayor-1 well (correlated with ATNTS2012 reversals and some key isotope stages), Carmona A and D sections, and reference sections from the Sicilian succession (Capodarso Tripoli, Realmonte clay layer within halite, Racalmuto clay layers within halite, Eraclea Minoa marly levels intercalated with gypsum beds, Eraclea Minoa Lago Mare Formation, Eraclea Minoa Arenazzolo Formation, Capo Rossello Trubi). Compared climatic quantification (MAT and MAP) of the Carmona with those of Sicily (pre-MC, 1st step MC, post-MC) and a part of Montemayor-1 (MC paroxysm), which are climatostratigraphically correlated with the Montemayor-1 oxygen isotopic curve. Three Sicilian sections, Capodarso (Tripoli), Racalmuto (halite) and Capo Rossello (Trubi) are also correlated with ATNTS2012 (Hilgen, 1991; Gautier *et al.*, 1994). Legend of pollen groups, see Figure 6.

Fig. 10. Comparaison entre les diagrammes polliniques synthétiques du bassin du Guadalquivir et ceux de Sicile ainsi qu'entre leur quantification paléoclimatique respective.

6.2 Compared Eastern Atlantic and Mediterranean sea-level

The global sea-level curve published by Miller *et al.* (2011), is built on benthic foraminiferal $\delta^{18}O$ data. Reproduced in Figure 7 for the time-interval encompassing the MC, this curve shows a maximum range in variability of 50 m only. However, it displays an outline to which a comparison of the Montemayor-1 D/P curve is useful (Fig. 7). In Figure 7, we reproduce the curve named 'modified H05' of Pérez-Asensio (2021) plotted on our age model. This curve provides estimated water depth based on foraminifer study from an important part of the Montemayor-1 well. Its large frequency fluctuations are almost consistent with those of D/P curve but they show a greatly detailed variability in addition to estimated values.

According to the D/P ratio, a progressive sea-level fall is reported from ~5.87 Ma to ~5.70 Ma, followed by a sea-level rise from ~5.70 to ~5.63 Ma, then by another discontinuous fall up to ~5.49 Ma before another rise from ~5.49 to ~5.32 Ma when it was followed by a new fall. This succession supports the correlations proposed with the Montemayor-1 D/P curve and the Carmona chronostratigraphy (Fig. 7). Particularly, the correlation of the Caliza Tosca with the interval 5.87–5.60 Ma seems well tied. Similarly, the subaerial erosion evidenced at Carmona appears consistent with the sea-level evolution during the interval 5.60–5.49 Ma although the global sea-level drop is interrupted by a brief rise during the lower part of the interval as also detectable in the Montemayor-1 D/P curve (Fig. 7). More accurately, the water depth reconstruction (Pérez-Asensio, 2021) exhibits a rapid and meaningful fall in sea-level of ca. 55 m at 5.60 Ma (Fig. 7). Despite its uncertainty, this value is inferior in about 60 m to that indicated by field observations, that leads to also involve some tectonic interaction. The water depth reconstruction evidences several subsequent positive fluctuations resulting in a more stable higher sea level at about 5.49 Ma that we correlate with the Nested Sandstone Fm. of Carmona (Fig. 7). It is not excluded that overflowing conditions upstream Carmona linked to global sea-level rise locally accentuated by the above-mentioned release of the olistostrome advance.

Both our estimate of the 5.60 Ma sea-level fall at Carmona and that at Montemayor-1 exceed the value proposed by Miller *et al.* (2011). Despite the difference in amplitude of the global sea-level fluctuations, the chronology and outline of the oxygen isotopic curve provide the base for correlations with the Mediterranean events as expressed in Figure 7: accordingly, the correlations with the Messinian events in the Mediterranean proposed by Jiménez-Moreno *et al.* (2013) can be specified, especially in ending the MC at 5.46 (Bache *et al.*, 2012; Popescu *et al.*, 2021), *i.e.* just after the global sea-level rise at ~5.49 Ma to which we correlate the base of the Carmona Nested Sandstone Fm. (Fig. 7).

6.3 The Messinian erosion in the Western Alboran area

The outstanding scale of the fluvial erosion during the second step of the MC is abundantly documented onshore and

offshore in the Mediterranean Basin and the adjacent Paratethys (Fig. 1B; *e.g.*: Clauzon, 1978, 1982; Ryan and Cita, 1978; Delrieu *et al.*, 1993; Rubino *et al.*, 2010; Clauzon *et al.*, 2005, 2015a-b; Gorini *et al.*, 2005; Lofi *et al.*, 2005; Manzi *et al.*, 2007; Bache *et al.*, 2009; Melinte-Dobrinescu *et al.*, 2009; Do Couto *et al.*, 2014; Suc *et al.*, 2015a-b; Cornée *et al.*, 2014, 2016; Pellen *et al.*, 2017, 2019; Amadori *et al.*, 2018; Madof *et al.*, 2019). In the onshore Sorbas Basin (Fig. 2), located eastward of the perched WAB (Fig. 1B; Booth-Rea *et al.*, 2018), the Messinian Erosional Surface has been quantified with an extent of ~150 m in an almost similar situation than the Carmona Messinian valley with respect to the paleo-river source (Do Couto *et al.*, 2015). This extent is consistent with the measured erosion of about 114 m at Carmona. In the WAB, the imprint of erosion is distinct in the back of Messinian valleys (Fig. 9), likewise in Sorbas and other Mediterranean locations. This context allows to propose for the WAB the following geodynamic evolution between 6.3 and 5.2 Ma:

- contrarily to the whole Mediterranean, there is no peripheral evaporite exposed onshore around the WAB (Fig. 1A) in correspondence with the first step of the MC (5.97–5.60 Ma) despite the Atlantic-level drop illustrated by the Caliza Tosca at Carmona;
- at the beginning of the second step of the MC (5.60 Ma), the Atlantic-level drop contributed to the onset of the desiccation process in the Mediterranean including the WAB as supported by the erosional surface observed on its two shorelines);
- rapidly, the WAB was isolated from the Mediterranean and continued to connect with the Atlantic Ocean probably thanks to the reactivation of its volcanic arc in relation with the isostatic readjustement due to the almost complete evaporation in the Mediterranean (Sternai *et al.*, 2017); this event probably stopped the erosional progression in the WAB with the support of a rise in global sea-level at 5.55 Ma (Fig. 7), explaining also why there is no central evaporite here (Fig. 1B);
- at 5.46 Ma (Bache *et al.*, 2012), the volcanic arc isolating the WAB was suddenly eroded by the Atlantic stream (Fig. 1B; Blanc, 2002; Garcia-Castellanos *et al.*, 2009) in relation both with the global sea-level rise (Fig.7; Miller *et al.*, 2011) and weakening of the volcanic activity maybe in relation with lithospheric loading by the central Mediterranean evaporites (Govers *et al.*, 2009; Sternai *et al.*, 2017).

This scenario is consistent with that elaborated for the entire Mediterranean by Bache *et al.* (2012, 2015) and that for the Apennine foredeep (Pellen *et al.*, 2017, 2022,) to which the isolation of the WAB during a part of the MC paroxysm resembles.

Even if our calculation of Atlantic sea-level fall of about 114 m at Carmona may be somewhat overestimated because of the syn-MC isostatic readjustements resulting from the desiccation phase followed by central evaporite deposition (Bache *et al.*, 2015), albeit the place is relatively far from the Mediterranean margin (Govers *et al.*, 2009), and considering that the Rifian Corridor was closed long before the MC (Capella *et al.*, 2018), we believe that the paroxysm of the crisis was most likely caused by a conjunction of regional (tectonic) and global (eustatic and tectonic) events making an impressive episode at the scale of the Earth (Warny *et al.*, 2003; Ohneiser *et al.*, 2015; Leroux *et al.*, 2018).

Messinian marine sediments are recorded in several industry or research wells in the WAB where the Messinian-Zanclean boundary is considered to be a paraconformity (Booth-Rea *et al.*, 2018; Gómez de la Peña *et al.*, 2021). Biostratigraphy of the ODP Site 976B has been recently refined, suggesting a possible continuous sedimentation from Messinian to Zanclean (Popescu *et al.*, 2015; Bulian *et al.*, 2021). Validation of the perched WAB hypothesis (Booth-Rea *et al.*, 2018) should be one of the challenges of the forthcoming IODP Leg 401.

6.4 Compared climate from Eastern Atlantic and Central Mediterranean

The summary pollen diagram of the Montemayor-1 hole presented in Figure 10 covers the time-interval from ~6.30 to ~5.20 Ma, which encompasses the whole MC in the Mediterranean and is characterized by a reliable chronology (Jiménez-Moreno *et al.*, 2013), allowing chronostratigraphic relationships with the Sicilian pollen records. The climate evolution displayed by the Montemayor-1 summary pollen diagram is relatively discrete because changes in vegetation linked to climate are slightly contrasted due to the great prevalence of herbaceous plants and Mediterranean sclerophyllous elements indicating continuous dry conditions (Fig. 10):

- a cooling is observed from 6.03 to ~5.75 Ma according to rarefying thermophilous plants and expanding *Cathaya* (an altitudinal tree in subtropical China today);
- warmer conditions existed between ~5.75 and ~5.60 Ma, indicated by increased thermophilous plants (including Mediterranean sclerophyllous elements);
- drier conditions developed after ~5.60 Ma, supported by scarcity of the trees requiring humid conditions; climate parameters have been quantified from the most significant samples of this interval which corresponds to the MC paroxysm in the Mediterranean Basin (Tab. S3);
- return to a less dry context after ~5.30 Ma, as shown by increased percentages of plants requiring humidity.

The Carmona A and D pollen records indeed represent only a small part of the Montemayor-1 record (Fig. 10) but, thanks to their deposition in a coastal setting, provide a larger number of pollen grains and show a significantly richer plant diversity (*i.e.* 141 vs. 90 taxa, respectively; Tab. S1).

Using pollen data, the climate has been quantified from the early Messinian to early Zanclean along the Sicilian series except during the crisis paroxysm (5.60–5.46 Ma) (Tab. S3; Fauquette *et al.*, 2006). According to paleogeographic reconstructions, the Carmona area and the South Sicily were located at almost the same paleolatitude (37–37°30'N) during the late Messinian (Jolivet *et al.*, 2006; Pellen *et al.*, 2022). Chronostratigraphy of the Sicilian succession refers (1) to the

ATNTS2012 (Capodarso: Gautier *et al*., 1994; Suc *et al*., 1995; Capo Rossello: Hilgen, 1991) and (2) to the time scale proposed by Clauzon *et al*. (1996) and specified by Bache *et al*. (2012), Manzi *et al*. (2013) and Popescu *et al*. (2021) for the MC (Fig. 10).

The Carmona pollen records may be compared to the Sicilian records during two periods (~6.25–6.05 Ma and ~5.32–5.29 Ma; *i.e*. parts of the Capodarso (Tripoli) and Capo Rossello (Trubi) records, respectively; (Fig. 10; Tabs. S2, S3):

- during the first period (~6.25–6.05 Ma), MAT at Carmona mostly ranged between ~18.1 and 20.5°C except the above-mentioned minimum at ~16°C and maxima at 22.4°C while South Sicily MAT mostly ranged between 20.6 and 23.6°C except a maximum at 24.5°C and three minima at 19.3, 19.9 and 20°C; MAP at Carmona mostly ranged between 520 and 870 mm except two maxima >1,100 mm and four minima <400 mm while South Sicily MAP ranged between ~780 and 1,020 mm except two minima at 430-450 mm; South Sicily was warmer but less dry than the Carmona area;
- during the second period (~5.32–5.29 Ma), MAT at Carmona mostly ranged between 19.4 and 22.3°C except the above-mentioned minimum at 15.5°C and two maxima at 22.9 and 24°C while South Sicily MAT mostly ranging between 18.7 and 20.2°C except two maxima above 24°C; MAP at Carmona mostly ranged between 360 and 680 mm except two maxima at 780 and 810 mm while Sicily MAP ranged between 453 and 625 mm except a maximum at 792 mm; the Carmona area was warmer than South Sicily and the dryness was similar in the two regions.

At Carmona, the post-MC temperature was higher than the pre-MC one, consistently with the global temperature illustrated by the oxygen isotopic curve (Fig. 10) but precipitation significantly decreased when comparing the two periods. In South Sicily, temperature surprisingly decreased when comparing the pre-MC and the early Zanclean conditions although the temperature revealed by the Arenazzolo (Eraclea Minoa) pollen record was much higher in correspondence with the context ending the MC. In both regions, post-MC precipitation was lower than before the crisis. This could be interpreted as resulting from the onset of a new regime in atmospheric circulation after changes in the Antarctic glaciations as seen occurring in the Mid-Miocene from pollen data combined to hydrogen isotopes from leaf waxes (Feakins *et al*., 2012).

Basically, a dry southern latitudinal zone pre-existed the MC for a long time, as suggested by simulated vegetation maps (Favre *et al*., 2007), which made the Mediterranean Sea climatically predisposed to desiccation (Fauquette *et al*., 2006). Glacio-eustatic sea-level falls recorded in the Antarctic region probably contributed to the two steps of the MC as proposed by Ohneiser *et al*. (2015) but that at 5.60 Ma had a greater effect on the region of the Gibraltar Strait (ca. 114 m) than predicted by these authors (50 m only). In contrast with the Ohneiser *et al*.'s claim, there are irrefutable field evidences showing that the marine reflooding of the Mediterranean Basin occurred long before the beginning of the Zanclean Stage (Cavazza and DeCelles, 1998; Bache *et al*., 2012; Popescu *et al*., 2021; van Dijk *et al*., 2023). The age of the Mediterranean marine reflooding at ~5.46 Ma suggests that its cause sets in the erosion of the West Alboran volcanic arc by Atlantic waters maybe as a consequence of the global sea-level rise that occurred just before (Miller *et al*., 2011).

Only two pollen records from Eastern Atlantic locations at South Mediterranean latitudes can be considered for reconstructing climate parameters during the paroxysm of the MC: Bou Regreg in Northwestern Morocco (Warny and Wrenn, 1997; Warny, 1999; Warny *et al*., 2003; Fauquette *et al*., 2006) and Montemayor-1 hole (Jiménez-Moreno *et al*., 2013). At Bou Regreg, estimated MAT generally oscillates between 19 and 22°C during the paroxysmic stage and MAP between 400 and 450 mm (Fauquette *et al*., 2006). Such values are consistent with those estimated in Sicily just before the paroxysm (Eraclea Minoa Lago Mare; Fig. 10). At Montemayor-1, MAT is estimated between 18 and 20°C, and MAP is estimated between 390 and 470 mm. Dry conditions obtained in Northwestern Morocco and Guadalquivir during the MC paroxysm may be explained by the desiccation in the Mediterranean region. Climate conditions have been simulated in the context of an almost completely desiccated Mediterranean Basin during the MC paroxysm (LS simulation: Murphy *et al*., 2009), resulting in even drier conditions in Sicily than in the Eastern Atlantic regions (Guadalquivir, Morocco). The climate conditions in the Mediterranean central basins during the MC paroxysm are still undocumented by pollen data and actually unknown. They were probably excessively arid because they led to the northward migration of subdesertic plants (Fauquette *et al*., 2006) by more than 6° in latitude according to paleogeographic reconstructions (Pellen *et al*., 2022). Sedimentary successions from the perched isolated basins may alone inform on climate of the MC paroxysm as done by the Maccarone record from the northern Apennine foredeep (Fauquette *et al*., 2006). If the WAB was really a perched basin during the MC paroxysm, new information is to be expected from imminent drillings (IODP Leg 401).

7 Conclusion

Past and new field investigations performed at Carmona lead to evidence two successive falls of the Atlantic sea-level in shallow coastal deposits, the latter of which generated a subaerial erosion contrasting with the deep submarine erosion known in the Guadalquivir Basin. Chronology of these events is supported by lithostratigraphy, biostratigraphy and magnetostratigraphy of exposed and cored sections completing former industrial seismic profiles and wells. The older sea-level fall is illustrated by the coastal Caliza Tosca calcarenite, which is correlated with the first step of the MC in the Mediterranean. The younger sea-level fall is expressed by a fluvial erosion, with a measured amplitude of about 114 m. The second and paroxysmal step of the MC is correlated to this fall of sea-level whose the amplitude is presumably to be moderated with regard to water depth estimates at the Montemayor-1 well, maybe because of the regional isostatic readjustements linked to the MC paroxysm and the sudden subsequent marine reflooding. A high-energy sandstone formation is nested within the older deposits and indicates a significant rise of global sea level at ca. 5.49 Ma. The submarine erosional event occurred just before the beginning of the Pliocene and must be

exclusively referred to the strain exerted by the Guadalquivir olistostrome. A critical result of this study is to succeed to discriminate context and age of the two successive erosional events at Carmona.

Pollen content of the Carmona sections and the MAT curve obtained from its paleoclimatic quantification allow climatostratigraphic relationships with the oxygen isotope curve of the Montemayor-1 hole within the pre-established biostratigraphic and magnetostratigraphic frame. The D/P (total dinoflagellate cysts/total pollen grains) ratio and a re-visited bathymetric reconstruction also document the variations of sea level and complete the correlations between the Carmona sections and the Montemayor-1 hole, tied to the global sea-level curve. The correlation of these events recorded in the Guadalquivir region and the Mediterranean events evidences that changes in global sea level have contributed to the onset and the end of the MC in the Mediterranean region.

The regional paleogeography was re-interpreted thanks to the established opening of the Gibraltar Strait long before the Messinian events and by the hypothesized West Alboran Basin connected to the Atlantic Ocean and isolated from the rest of the Mediterranean Basin by a volcanic barrier during the most of the MC paroxysm.

Comparison of quantified paleoclimate data derived from pollen records of the Guadalquivir region and Sicily confirms that the Southern Mediterranean region *s.l.* was subjected to dry conditions and thus climatically predisposed to desiccation, which supports the assumption of some inference of global eustatism to begin and end the MC.

Supplementary material

Table S1: Detailed pollen and spore analyses of Carmona D and Carmona A sections, produced from top to base.

Table S2: Quantified climate from pollen analyses of Carmona D and Carmona A sections. MAT refers to mean annual temperature; MTC to mean temperature of the coldest month; MTW to mean temperature of the warmest month; MAP to mean annual precipitation; and MLV to the most likely value, *i.e.* a weighted mean for each parameter.

Table S3: Quantified climate from pollen analyses of the Sicilian sections and a portion of the Montemayor-1 hole organized with respect to chronology. Same legend as Table S2.

The Supplementary Material is available at https://www.bsgf.fr/10.1051/bsgf/2023013/olm.

Acknowledgements. The late G. Clauzon actively contributed to two field trips, particularly in evidencing the valley fill including the Nested Sandstone Formation. E.J. Mayoral guided us on the field. P. Guenet handled the coring process. The late F. Gautier contributed to the coring campaign, especially in paleomagnetic logging and measurements in Grenoble. J. Pocachard and T. Thomas (LETI-CEA, Grenoble) contributed in providing the paleomagnetism logging material used *in situ* and access to the measurement bed in Grenoble. Some additional information on foraminifera and paleomagnetism were provided by F.J. Sierro and W. Krijgsman, respectively. The coring campaign was financially supported by CNRS-INSU, Total and Elf-Aquitaine companies. We particularly appreciated the comments and suggestions addressed by the two referees, P. Sternai and G. Booth-Rea.

References

Achalhi M, Münch P, Cornée J-J., Azdimousa A, Melinte-Dobrinescu M, Quillévéré F *et al.* 2016. The late Miocene Mediterranean-Atlantic connections through the North Rifian Corridor: new insights from the Boudinar and Arbaa Taourirt basins (northeastern Rif, Morocco). Palaeogeogr Palaeoclimatol Palaeoecol 459: 131–152.

Aguirre E, Menéndez Amor J, Lhénaff R, Alférez F, Maco J. 1967. El Mioceno superior (Andaluciense) en Sevilla y Cadiz. 4th Congress of the Committee of the Mediterranean Neogene. Bologne, 19 p.

Aguirre J, Braga JC, Martín JM, Puga-Bernabéu Á, Pérez-Asensio J, Sánchez-Almazo I *et al.* 2015. An enigmatic kilometre-scale concentration of small mytilids (Late Miocene, Guadalquivir Basin, S Spain). Palaeogeogr Palaeoclimatol Palaeoecol 436: 199–213.

Amadori C, Garcia-Castellanos D, Toscani G *et al.* 2018. Restored topography of the Po Plain-Northern Adriatic region during the Messinian base-level drop-Implications for the physiography and compartmentalization of the palaeo-Mediterranean basin. *Basin Res* 30: 1247–1263.

Anthonissen DE, Ogg JG. 2012. Cenozoic and Cretaceous biochronology of planktonic foraminifera and calcareous nannofossils. In Gradstein FM, Ogg JG, Schmitz MD, Ogg GM, eds. The geologic time scale 2012. Amsterdam (The Netherlands): Elsevier, pp. 1083–1127.

Bache F, Gargani J, Suc J- P *et al.* 2015. Messinian evaporite deposition during sea level rise in the Gulf of Lions (Western Mediterranean). *Mar Pet Geol* 66: 262–277.

Bache F, Olivet J-L, Gorini C *et al.* 2009. Messinian erosional and salinity crises: view from the Provence Basin (Gulf of Lions, Western Mediterranean). *Earth Planet Sci Lett* 286: 139–157.

Bache F, Popescu S-M, Rabineau M *et al.* 2012. A two-step process for the reflooding of the Mediterranean after the Messinian Salinity Crisis. *Basin Res* 24: 125–153.

Berggren WA, Haq BU. 1976. The Andalusian Stage (Late Miocene): biostratigraphy, biochronology and paleoecology. *Palaeogeogr Palaeoclimatol Palaeoecol* 20: 67–129.

Blanc P-L. 2002. The opening of the Plio-Quaternary Gibraltar Strait: assessing the size of a cataclysm. *Geodin Acta* 15: 303–317.

Booth-Rea G, Ranero CR, Grevemeyer I. 2018. The Alboran volcanic-arc modulated the Messinian faunal exchange and salinity crisis. *Sci Rep* 8: 13015.

Borrero Dominguez JD, Roldán García FJ. 1985. Carmona. Mapa Geológico de España at scale 1:50,000, 985 (13-40), Madrid : Instituto Geológico y Minero de España.

Bulian F, Sierro FJ, Ledesma S, Jiménez-Espejo FJ, Bassetti M-A. 2021. Messinian West Alboran Sea record in the proximity of Gibraltar: early signs of Atlantic-Mediterranean gateway restriction. *Mar Geol* 434: 106430.

Capella W, Barhoun N, Flecker R *et al.* 2018. Palaeogeographic evolution of the late Miocene Rifian Corridor (Morocco): reconstructions from surface and subsurface data. *Earth-Sci Rev* 180: 37–59.

Cavazza W, DeCelles PG. 1998. Upper Messinian siliciclastic rocks in southeastern Calabria (southern Italy): paleotectonic and eustatic implications for the evolution of the central Mediterranean region. *Tectonophysics* 298: 223–241.

Civis J, Dabrio CJ, González-Delgado JA *et al.* 2004. Cuenca del Guadalquivir. In: Vera JA, ed. Madrid (Spain): Geología de España. Instituto Geológico y Minero de España and Sociedad Geológica de España, pp. 543–550.

Clauzon G. 1978. The Messinian Var canyon (Provence, Southern france) – Paleogeographic implications. *Mar Geol* 27: 231–246.
Clauzon G. 1982. Le canyon Messinien du Rhône: une preuve décisive du "desiccated deep-basin model" [Hsü, Cita et Ryan, 1973]. *Bull Soc Géol Fr* 24(3)(S7):597–610.
Clauzon G, Le Strat P, Duvail C *et al*. 2015b. The Roussillon Basin (S. France): a case-study to distinguish local and regional events between 6 and 3 Ma. *Mar Pet Geol* 66: 18–40.
Clauzon G, Suc J-P, Do Couto D *et al*. 2015a. New insights on the Sorbas Basin (SE Spain): The onshore reference of the Messinian Salinity Crisis. *Mar Pet Geol* 66: 71–100.
Clauzon G, Suc J-P., Gautier F, Berger A. Loutre M-F. 1996. Alternate interpretation of the Messinian salinity crisis: controversy resolved? *Geology* 24: 363–366.
Clauzon G, Suc J-P, Popescu S-M *et al*. 2005. Influence of Mediterranean sea-level changes on the Dacic Basin (Eastern Paratethys) during the late Neogene: the Mediterranean Lago Mare facies deciphered. *Basin Res* 17: 437–462.
Climate data for cities worldwide. Available from https://en.climate-data.org (last consult: 2023 /09/07).
Cornée J-J., Münch P, Achalhi M *et al*. 2016. The Messinian erosional surface and early Pliocene reflooding in the Alboran Sea: new insights from the Boudinar Basin, Morocco. *Sediment Geol* 333: 115–129.
Cornée J-J., Münch P, Melinte-Dobrinescu MC *et al*. 2014. The Early Pliocene reflooding in the Western Mediterranean: new insights from the rias of the Internal Rif, Morocco. *CR Geosci* 346: 90–98.
Delrieu B, Rouchy J-M., Foucault A. 1993. La surface d'érosion finimessinienne en Crète centrale (Grèce) et sur le pourtour méditerranéen: rapports avec la crise de salinité méditerranéenne. *CR Acad Sci Paris* 316(S2): 527–533.
Do Couto D, Gumiaux C, Jolivet L *et al*. 2015. 3D modelling of the Sorbas Basin (Spain): new constraints on the Messinian Erosional Surface morphology. *Mar Pet Geol* 66: 101–116.
Do Couto D, Popescu S-M, Suc J-P *et al*. 2014. Lago Mare and the Messinian Salinity Crisis: evidence from the Alboran Sea (S. Spain). *Mar Pet Geol* 52: 57–76.
Fauquette S, Guiot J, Suc J-P. 1998. A method for climatic reconstruction of the Mediterranean Pliocene using pollen data. *Palaeogeogr Palaeoclimatol Palaeoecol* 144: 183–201.
Fauquette S, Suc J-P, Bertini A *et al*. 2006. How much did climate force the Messinian salinity crisis? Quantified climatic conditions from pollen records in the Mediterranean region. *Palaeogeogr Palaeoclimatol Palaeoecol* 238: 281–301.
Favre E, Escarguel G, Suc J-P., Vidal G, Thévenod L. 2008. A contribution to deciphering the meaning of AP/NAP with respect to vegetation cover. *Rev Palaeobot Palynol* 148: 13–35.
Favre E, François L, Fluteau F, Cheddadi R, Thévenod L, Suc J-P. 2007. Messinian vegetation maps of the Mediterranean region using models and interpolated pollen data. *Geobios* 40: 433–443.
Feakins SJ, Warny S, Lee JE. 2012. Hydrologic cycling over Antarctica during the middle Miocene warming. *Nat Geosci* 5: 557–560.
Garcia-Castellanos D, Estrada F, Jiménez-Munt I *et al*. 2009. Catastrophic flood of the Mediterranean after the Messinian salinity crisis. *Nature* 462: 778–781.
Gautier F, Clauzon G, Suc J-P., Cravatte J, Violanti D. 1994. Age et durée de la crise de salinité messinienne. *CR Acad Sci Paris* 318 (S2): 1103–1109.
Gómez de la Peña L, Ranero CR, Gràcia E, Booth-Rea G. 2021. The evolution of the westernmost Mediterranean basins. *Earth-Sci Rev* 214: 103445.
Gorini C, Lofi J, Duvail C et al. 2005. The late Messinian salinity crisis and Late Miocene tectonism: interaction and consequences on the physiography and post-rift evolution of the Gulf of Lions margin. *Mar Pet Geol* 22: 695–712.
Govers R, Meijer P, Krijgsman W. 2009. Regional isotatic response to Messinian Salinity Crisis events. *Tectonophysics* 463: 109–129.
Hilgen FJ. 1991. Extention of the astronomically calibrated (polarity) time scale to the Miocene/Pliocene boundary. *Earth Planet Sci Lett* 107: 349–368.
Hilgen FJ, Lourens LJ, Van Dam JA. 2012. The Neogene period. In Gradstein FM, Ogg JG, Schmitz MD, Ogg GM, eds. The geologic time scale 2012. Amsterdam (The Netherlands): Elsevier, 2012, pp. 923–978.
Hodell DA, Benson RH, Kent DV, Boersma A, Rakic-El Bied K. 1994. Magnetostratigraphy, biostratigraphic, and stable isotope stratigraphy of an Upper Miocene drill core from Salé Briqueterie (northwestern Morocco): a high-resolution chronology for the Messinian stage. *Paleoceanography* 9: 835–855.
Iaccarino SM, Bertini A, Di Stefano A *et al*. 2008. The Trave section (Monte dei Corvi, Ancona, Central Italy): an integrated paleontological study of the Messinian deposits. *Stratigraphy* 5 (3-4): 281–306.
Jiménez-Moreno G, Head MJ, Harzauser M. 2006. Early and liddle Miocene dinoflagellate cyst stratigraphy of the central Paratethys-Central Europe. *J Micropaleontol* 25: 113–139.
Jiménez-Moreno G, Pérez-Asensio JN, Larrasoaña JC *et al*. 2013. Vegetation, sea-level, and climate changes during the Messinian salinity crisis. *Geol Soc Am Bull* 125: 432–444.
Jolivet L, Augier R, Robin C, Suc J-P., Rouchy JM. 2006. Lithospheric-scale geodynamic context of the Messinian salinity crisis. *Sediment Geol* 188-189: 9–33.
Krijgsman W, Capella W, Simon D *et al*. 2018. The Gibraltar Corridor: Watergate of the Messinian Salinity Crisis. *Mar Geol* 404: 238–246.
Krijgsman W, Hilgen FJ, Raffi I, Sierro FJ, Wilson DS. 1999. Chronology, causes and progression of the Messinian salinity crisis. *Nature* 400: 652–655.
Krijgsman W, Fortuin AR, Hilgen FJ, Sierro FJ. 2001. Astrochronology for the Messinian Sorbas basin (SE Spain) and orbital (precessional) forcing for evaporite cyclicity. *Sediment Geol* 140: 41–60.
Ledesma S. 2000. Astrobiocronología y estratigrafía de alta resolución del Neógeno de la Cuenca Guadalquivir-Golfo de Cádiz. PhD thesis, University of Salamanca. Available from https://gredos.usal.es/bitstream/10366/141065/1/DGL_LedesmaMateo%202000.pdf (last consult: 2023/09/07).
Leroux E, Aslanian D, Rabineau M, Pellen R, Moulin M. 2018. The late Messinian event: a worldwide tectonic revolution. *Terra Nova* 30: 207–214.
Lofi J, Gorini C, Berné S *et al*. 2005. Erosional processes and paleo-environmental changes in the Western Gulf of Lions (SW France) during the Messinian Salinity Crisis. *Mar Geol* 217: 1–30.
Madof AS, Bertoni C, Lofi J. 2019. Discovery of vast fluvial deposits provides evidence for drawdown during the late Miocene Messinian salinity crisis. *Geology* 47: 171–174.
Magné J, Viguier C. 1974. Stratigraphie du Néogène marin "post-nappe" de l'Andalousie occidentale. *Mémoires du Bureau de Recherches Géologiques et Minières* 78 (2): 821–827.
Manzi V, Gennari R, Hilgen F *et al*. 2013. Age refinement of the Messinian salinity crisis onset in the Mediterranean. *Terra Nova* 25: 315–322.

Manzi V, Roveri M, Gennari R *et al*. 2007. The deep-water counterpart of the Messinian Lower Evaporites in the Apennine foredeep: the Fannantello section (Northern Apennines, Italy). *Palaeogeogr Palaeoclimatol Palaeoecol* 251: 470–499.

Martínez del Olmo WM, Martín D. 2016a. El Neógeno de la Cuenca Guadalquivir-Cádiz (Sur de España). *Revista de la Sociedad Geológica de España* 29: 35–58.

Martínez del Olmo WM, Martín D. 2016b. The Messinian record of Spanish onshore and offshore data (Atlantic Ocean and Western Mediterranean Sea). *Pet Geosci* 22: 291–296.

Martínez del Olmo WM, Riaza Molina C, Torrescusa Villaverde S. 1996. Descenso eustático messiniense en une cuenca atlántica. El cañón submarine del Río Guadalquivir (SO de España). *Geogaceta* 20: 138–141.

Martínez del Olmo WM, Sánchez DM. 2019. Surcos erosivos, sistemas de turbiditas y episodios climáticos en el Tortoniense y Messiniense de la Cuenca Guadalquivir (SO de España). *Revista de la Sociedad Geológica de España* 32: 97–112.

Melinte-Dobrinescu MC, Suc J-P, Clauzon G *et al*. 2009. The Messinian Salinity Crisis in the Dardanelles region: chronostratigraphic constraints. *Palaeogeogr Palaeoclimatol Palaeoecol* 278: 24–39.

Miller KG, Mountain GS, Wright JD, Browning JV. 2011. 80-Million-year record of level and ice volume variations from continental margin and deep-sea isotopic records. *Oceanography* 24 (2): 40–53.

Murphy LN, Kirk-Davidoff DB, Mahowald N, Otto-Bliesner BL. 2009. A numerical study of the climate response to lowered Mediterranean Sea level during the Messinian Salinity Crisis. *Palaeogeogr Palaeoclimatol Palaeoecol* 279: 41–59.

Néraudeau D. 2007. Les bioaccumulations néogènes (calcaires à algues, faluns) d'Europe occidentale et leurs relations avec la crise messinienne. *CR Palevol* 6: 59–71.

Néraudeau D, Goubert E, Lacour D, Rouchy JM. 2001. Changing biodiversity of Mediterranean irregular echinoids from the Messinian to Present-Day. *Palaeogeogr Palaeoclimatol Palaeoecol* 175: 43–60.

Néraudeau D, Roman J, Borghi E. 1999. Impact of the Messinian crisis on the Mediterranean echinoid fauna. In Candia Carnevali M, Bonasoro F, eds. Echinoderm Research. Rotterdam (The Netherlands): Balkema AA, pp. 355–360.

Ogg JG. 2012. Geomagnetic polarity time scale. In Gradstein FM, Ogg JG, Schmitz MD, Ogg GM eds. The Geologic Time Scale 2012. Amsterdam (The Netherlands): Elsevier, pp. 85–113.

Ohneiser C, Florindo F, Stocchi P, Roberts AP, DeConto RM, Pollard D. 2015. Antarctic glacio-eustatic contributions to late Miocene Mediterranean desiccation and reflooding. *Nat Commun* 6: 8765.

Pellen R, Aslanian D, Rabineau M *et al*. 2019. The Messinian Ebro River incision. *Glob Planet Change* 181: 102988.

Pellen R, Aslanian D, Rabineau M *et al*. 2022. Structural and sedimentary origin of the Gargano-Pelagosa Gateway and impact on sedimentary evolution during the Messinian Salinity Crisis. *Earth-Sci Rev* 232: 104114.

Pellen R, Popescu S-M, Suc J-P *et al*. 2017. The Apennine foredeep (Italy) during the latest Messinian: Lago Mare reflects competing brackish and marine conditions based on calcareous nannofossils and dinoflagellate cysts. *Geobios* 50: 237–257.

Perconig E. 1974. Mise au point du stratotype de l'Andalousien. *Mémoires du Bureau de Recherches Géologiques et Minières* 78 (2): 664–673.

Perconig E, Martínez-Fresneda F. 1977. Sobre la heterocronia de la "Caliza Tosca" en el Mioceno superior de Andalucia occidental. Messinian Seminar n° 3, Malaga (Spain) UNESCO – IUGS IGCP Project n° 96 Messinian Correlation, 7 pp.

Pérez-Asensio JN. 2021. Quantitative palaeobathymetric reconstructions based on foraminiferal proxies: a case study from the Neogene of South-West Spain. *Palaeontology* 64: 475–488.

Pérez-Asensio JN, Aguirre J, Schmiedl G, Civis J. 2012. Messinian paleoenvironmental evolution in the lower Guadalquivir Basin (SW Spain) based on benthic foraminifera. *Palaeogeogr Palaeoclimatol Palaeoecol* 326-328: 135–151.

Popescu S-M., Cavazza W, Suc J-P., Melinte-Dobrinescu MC, Barhoun N, Gorini C. 2021. Pre-Zanclean end of the Messinian Salinity Crisis: new evidence from Central Mediterraneran reference sections. *J Geol Soc* 178 (3): jgs 2020–183.

Popescu SM, Dalibard M, Suc JP *et al*. 2015. Lago Mare episodes around the Messinian-Zanclean boundary in the deep southwestern Mediterranean. *Mar Pet Geol* 66: 55–70.

Pozzi J-P., Barthès V, Thibal J, Pocachard J, Lim M, Thomas T *et al*. 1993. Downhole magnetostratigraphy in sediments: comparison with the paleomagnetism of a core. *J Geophys Res* 98: 7939–7957.

Rico-García A. 2007. El Neógeno superior marino en Vejer de la Frontera (Cádiz, SO España) y su evolución regresiva. *Geogaceta* 42: 115–118.

Rubino J-L., Haddadi N, Camy-Peyret J *et al*. 2010. Messinian salinity crisis expression along North African margin. Society of Petroleum Engineers Conference, Le Caire, 129526–PP.

Ryan WBF, Carbotte SM, Coplan JO *et al*. 2009. Global multi-resolution topography synthesis. *Geochem Geophys Geosystems* 10: Q03014.

Ryan WBF, Cita MB. 1978. The nature and distribution of Messinian erosional surfaces-Indicators of a several-kilometer-deep Mediterranean in the Miocene. *Mar Geol* 27: 193–230.

Sierro FJ, Flores JA, Civis J, González Delgado JA, Francés G. 1993. Late Miocene globorotaliid event-stratigraphy and biogeography in the NE-Atlantic and Mediterranean. *Mar Micropaleontol* 21: 143–168.

Sierro FJ, González Delgado JA, Dabrio CJ, Flores JA, Civis J. 1990. The Neogene of the Guadalquivir Basin (SW Spain). *Paleontologia i Evolucio*, special issue 2: 209–250.

Sierro FJ, González Delgado JA, Dabrio CJ, Flores JA, Civis J. 1996. Late Neogene depositional sequences in the foreland basin of Guadalquivir (SW Spain). In Friend P, Dabrio CJ, eds. Tertiary Basins of Spain Cambridge (United Kingdom): Cambridge University press, pp. 339–345.

Sierro FJ, Ledesma S, Flores JA. 2008. Astrobiochronology of late Neogene deposits near the Strait of Gibraltar (SW Spain). Implications for the tectonic control of the Messinian Salinity Crisis. *CIESM Workshop Monographs* 33: 45–48.

Sternai P, Caricchi L, Garcia-Castellanos D, Jolivet L, Sheldrake TE, Castelltort S. 2017. Magmatic pulse driven by sea-level changes associated with the Messinian salinity crisis. *Nat Geosci* 10: 783–787.

Suc J-P., Bessais E. 1990. Pérennité d'un climat thermo-xérique en Sicile avant, pendant, après la crise de salinité messinienne. *CR Acad Sci Paris* 310(S2): 1701–1707.

Suc J-P., Gillet H, Çağatay MN *et al*. 2015a. The region of the Strandja Sill (North Turkey) and the Messinian events. *Mar Pet Geol* 66: 149–164.

Suc J-P., Gorini C, Rabineau M *et al*. 2019. Paleoenvironnements méditerranéens. 2, La Crise de salinité messinienne. *Géochronique* 151: 24–30.

Suc J-P., Popescu S-M., Do Couto D *et al*. 2015b. Marine gateways vs. fluvial stream within the Balkans from 6 to 5 Ma. *Mar Pet Geol* 66: 231–245.

Suc J-P., Violanti D, Londeix L *et al*. 1995. Evolution of the Messinian Mediterranean environments: the Tripoli Formation at Capodarso (Sicily, Italy). *Rev Palaeobot Palynol* 87: 51–79.

van den Berg BCJ, Sierro FJ, Hilgen FJ *et al*. 2018. Imprint of Messinian Salinity Crisis events on the Spanish Atlantic margin. *Newsl Stratigr* 51 (1): 93–115.

van der Laan E, Gaboardi S, Hilgen FJ, Lourens LJ. 2005. Regional climate and glacial control on high-resolution oxygen isotope records from Ain el Beida (latest Miocene, northwest Morocco): a cyclostratigraphic analysis in the depth and time domain. *Paleoceanography* 20: PA1001.

van der Laan E, Hilgen FJ, Lourens LJ, de Kaenel E, Gaboardi S, Iaccarino S. 2012. Astronomical forcing of Northwest African climate and glacial history during the late Messinian (6. 5- 5. 5 Ma). *Palaeogeogr Palaeoclimatol Palaeoecol* 313–314: 107-126.

van der Laan E, Snel E, de Kaenel E, Hilgen FJ, Krijgsman W. 2006. No major deglaciation across the Miocene-Pliocene boundary: integrated stratigraphy and astronomical tuning of the Loulja sections (Bou Regreg area, NW Morocco). *Paleoceanography* 21: PA3011.

van Dijk G, Maars J, Andreetto F, Hernández-Molina FJ, Rodríguez-Tovar J, Krijgsman W. 2023. A terminal Messinian flooding of the Mediterranean evidenced by contouritic deposits on Sicily. *Sedimentology* 70: 1195–1223.

Vera JA. 2000. El Terciario de la Cordillera Bética: estado actual de conocimientos. *Revista de la Sociedad Geológica de España* 13: 345–373.

Warny S. 1999. Marine and continental environment changes in the Gibraltar Arc area during the late Neogene (8–2. 7 Ma) linked to the evolution of global climate and to Atlantic Ocean-Mediterranean relationship. A palynological contribution to the Mediterranean Messinian Salinity Crisis through dinoflagellate cysts and pollen analysis. PhD thesis, Université Catholique de Louvain.

Warny SA, Wrenn JH. 1997. New species of dinoflagellate cysts from the Bou Regreg core: a Miocene-Pliocene boundary section on the Atlantic coast of Morocco. *Rev Palaeobot Palynol* 96: 281–304.

Warny SA, Bart PJ, Suc J-P. 2003. Timing and progression of climate, tectonic and glacioeustatic influences on the Messinian Salinity Crisis. *Palaeogeogr Palaeoclimatol Palaeoecol* 202: 59–66.

Cite this article as: Suc J-P, Fauquette S, Warny S, Jiménez-Moreno G, Do Couto D. 2023. Climate and Atlantic sea-level recorded in Southern Spain from 6.3 to 5.2 Ma. Inferences on the Messinian Crisis in the Mediterranean, *BSGF - Earth Sciences Bulletin* 194: 15.